

Using massless fields for observing black hole features in the collapsed phase of Euclidean dynamical triangulations

Jan Smit

Institute for Theoretical Physics, University of Amsterdam,
Science Park 904, P.O.Box 94485, 1090 GL Amsterdam, the Netherlands.

We report on an old computation of propagators of massless scalar fields on an ensemble of configurations in 4D Euclidean dynamical triangulations in the collapsed (crumpled) phase. The resulting quantum average is used to construct the scale factor of a 4-D rotational invariant metric. This new scale factor is non-zero at the origin, which we assume to be caused the presence of the well-known singular structure in the collapsed phase. The scale factor depends on an overall integration constant, which is determined by comparison with the implied volume at intermediate distances. We construct a transformation to a 3-D rotational invariant metric, which reveals Euclidean black hole features at an instant in time, with a horizon separating interior and exterior parts. Effective Einstein equations in the presence of a ‘geometric condensate’ are assumed, and computed with the software OGRE. Also explored briefly is a qualitatively different (not preferred) interpretation of the data which follows from comparison with an inversely transformed Euclidean regular black hole metric.

I. INTRODUCTION

In the dynamical triangulation approach to Euclidean quantum gravity (EDT) the configurations of the regulated path integral form a lattice consisting of equilateral four-simplexes ‘glued’ together [1–3] (for reviewing texts see e.g. [4–7]). A scenario for a continuum limit has been proposed [7] for a model with three parameters, two of which monitor the (bare) Newton and cosmological couplings, G_{N0} and Λ_0 , the third controls a ‘measure term’. This measure term is a local factor in the summation measure over configurations [8, 9] which can be written as a term in the action that depends logarithmically on the Regge curvature [5, 10] (initially a different one was introduced in [11], recently revisited in [12]).

A customary notation uses dimensionless parameters $\kappa_2 \propto 1/G_{N0}$ and $\kappa_4 \leftrightarrow \Lambda_0$, and β for the measure term. Numerical simulations have revealed two phases, a ‘collapsed phase’ (a.k.a. ‘crumpled phase’) at strong coupling and an ‘elongated phase’ at weak coupling, separated by a first-order transition line in the κ_2 - β phase diagram [6, 10, 13–15]. In the scenario of [7] the continuum limit is to be approached along the phase boundary on the collapsed side towards weaker couplings, i.e. larger κ_2 .

Similar phases appear in the formulation using well-defined time slices called ‘causal dynamical triangulation’ (CDT) [16–18], and approaches to a possible UV fixed point along ‘lines of constant physics’ are described in [19–21].

A continuum limit towards a phase boundary from the strong coupling side is also proposed in a different formulation with variable lattice edge lengths [22, 23].

The original EDT formulation had no measure term, i.e. $\beta = 0$ [1, 2]. Numerical simulations at $\beta = 0$ revealed that the two phases have very distinct properties. The elongated phase is dominated by baby universes with branched polymer characteristics [24]. Deep in the collapsed phase a ‘singular structure’ appears consisting of

two adjacent ‘singular vertices’ that belong to a macroscopic number of four-simplices that grows linearly with the lattice size [25–29]. Going towards weaker coupling the structure breaks up leaving only one singular vertex which finally disappears at the phase boundary [28].

Visualizations of typical configurations at $\beta = 0$ show fractal tree-like ‘branched-polymer’ structures in the elongated phase and a dense ‘blob’ with trees sticking out in the collapsed phase [6, 7, 15]. Branched polymers have been linked to conformal fields [30, 31] and one can imagine the blob as representing a naked singularity or a black hole, and the trees representing a boundary field theory, similar to AdS/CFT [32–34]. At negative β , upon increasing $-\beta$ and κ_2 the system enters a region called ‘crinkled’ [8, 9] in which the blob stratifies and includes larger distances [6, 10] with an accompanying smaller lattice spacing [7]. These features suggest studying quantal properties of black-holes by simulations in EDT.

At $\beta = 0$ there will be lattice artefacts in the results but they may still inform us about quantum-gravitational physics. The great advantage of the numerical simulations is that they yield truly non-perturbative results which can qualitatively and even semi-quantitatively describe physics. We recall that lattice QCD at strong coupling (i.e. far from its continuum limit) gives a fair characterization of the low mass hadrons (as summarized for example in [35], section 7.4).

In [36, 37] gravitational binding energy between two massive scalars was computed in EDT in the ‘quenched approximation’ (in perturbation theory this corresponds to leaving out closed particle loops). A non-zero binding energy E_b came out, with a dependence on the particle masses m that was not understood. A recent study [38] suggested an explanation in terms of a blow-up effect in the bound state wave function causing finite-size squeezing of the system with a *decreasing* ratio E_b/m with *increasing* m , in a large mass region. The effect is proportional to $m G_N$, with G_N a renormalized Newton

coupling. In an elaborate analysis of the results in [36] the renormalized Planck length $\sqrt{G_N}$ was estimated to be fairly large (≈ 8) in lattice units, near the phase transition on the collapsed side. The relevance of the black hole scale mG_N came as a surprise. (This explanation needs confirmation on larger lattices.)

A controlled computation of the binding energy appeared in [39]. This work used extrapolation to the continuum limit in the above mentioned scenario, scale-dependent dimensions allowing relatively small lattices and extrapolation to infinite volume, with the result $\sqrt{G_N} = 3.9 \pm 0.7$ in lattice units. A similar value was subsequently found using a completely different method [40]. These computations employed a different ensemble of so-called degenerate triangulations [3]. (In [38] the analysis uses dimension 4 which requires avoiding short distances.)

In [41] effective curvature observables based on a ‘volume-distance correlator’ were computed which showed at short distances negative curvature in the collapsed phase and positive curvature in the elongated phase.¹ This was refined further in [42] into effective *metrics* describing an average geometry.

The present work focuses on the collapsed phase *away* from the phase transition. We present results for the propagators of massless scalar-fields obtained from simulations in 1996 by B.V. de Bakker in collaboration with the present author. The negative curvature in the collapsed phase found earlier raised the question whether this would be ‘confirmed’ by an exponential decay of massless propagators at large distances, as in hyperbolic space in the continuum. Evidence for such decay was indeed found and briefly mentioned in [43], but for logistic reasons the write-up got stuck at the stage of ‘a draft of a draft’ [44]. Part of these results could be recovered recently. They are used here to derive, in a fundamentally different way, metrics for average geometries as observed through the propagators.

The propagator reacts to the quantum geometries in a way that fundamentally differs from the volume-distance observable. A clue to an explanation may be found in the plot in figure 2.7 of [45], which shows that a massless scalar field propagator on a configuration deep in the *elongated phase* becomes constant on the thin branches of its tree-like structure. It is reminiscent of the constancy of the electric potential in a Faraday cage.

Our knowledge of distances is based primarily on electrodynamics involving the massless photon, and on the Planck scale all fields in the Standard Model are practically massless.

The above mentioned volume-distance correlator is the average three-volume at a fixed distance from an arbitrary origin. With lattices of S^4 topology it leads natu-

rally to isotropic average metrics of the form

$$ds^2 = d\eta^2 + a(\eta)^2 d\Omega_3^2, \quad (1)$$

with $d\Omega_3$ the line-element on the unit three-sphere and η a radial coordinate in four dimensions.

In the continuum, the scale factor $a(\eta)$ is closely related to the derivative of the four-volume $V(\eta)$ within distance η from the origin:

$$V(\eta) = \int d\Omega_3 \int_0^\eta d\bar{\eta} a(\bar{\eta})^3, \quad \partial_\eta V(\eta) = 2\pi^2 a(\eta)^3. \quad (2)$$

On the lattice, a volume-distance correlator $V'(\eta)$ corresponding to $\partial_\eta V(\eta)$ has been used to construct a lattice version² of $a(\eta)$.

In the present work the important observable is the propagator $G(\eta)$ of a massless scalar field. In the continuum it has to satisfy the Laplace-Beltrami equation for the metric (1),

$$\left[\frac{d}{d\eta} + \frac{3}{a(\eta)} \frac{da(\eta)}{d\eta} \right] \frac{d}{d\eta} G(\eta) = 0, \quad \eta > 0, \quad (3)$$

with appropriate boundary conditions. Given $G(\eta)$, we can use (3) as a first-order differential equation for a scale factor $a(\eta)$. The solution is

$$a(\eta) = c_G a_G(\eta), \quad a_G(\eta) = \left[-\frac{1}{\partial_\eta G(\eta)} \right]^{1/3}, \quad (4)$$

with c_G an integration constant. Replacing the continuum $\partial_\eta G(\eta)$ by EDT data $G'(\eta)$ gives a new scale factor for the average quantum geometry.

The newly obtained scale factor $a(\eta)$ determines how the three-volume described by the metric grows with the distance from the origin, which depends on the integration constant c_G . We seek to determine c_G by comparison with the scale factor based on the volume-distance correlator $V(\eta)$. Both $G(\eta)$ and $V(\eta)$ involve a volume-average over the origin $\eta = 0$ and there will be branched-polymer contributions that are treated differently by the two observables. It turns out that at *medium distances*³ the ratio of the volumes described by the two different scale factors has a region of slow variation, a stationary point at which it may be set to one and thereby fix c_G .

A major characteristic of this new scale factor is that it suggests fit functions that are non-vanishing at the origin. Their extrapolation to the origin should not suffer greatly from lattice artefacts or running dimensions

¹ Negative curvature was also found in the strong coupling phase of the formulation with variable lattice edge lengths [22].

² Examples are given in appendices A and B. *Note that in appendices A, B, C and D, η is denoted by r — not to be confused with r in (5).*

³ The lattice scale factor $\propto V'(\eta)^{1/3}$ (interpolated) has a maximum at η_m and inflexion points η^\pm in $\eta \gtrsim \eta_m$. For clarity we define short, medium, transition and long distances respectively as $0 < \eta < \eta^-$, $\eta^- < \eta < \eta_m$, $\eta_m < \eta < \eta^+$ and $\eta^+ < \eta$.

and we assume this extrapolation to have physical significance.

To investigate whether the collapsed state has properties showing the presence of a black hole we make a transformation to spherical coordinates in which such objects have been traditionally introduced. The transformed line element has the form

$$ds^2 = g_{tt}(r, t)dt^2 + 2g_{rt}(r, t)dr dt + g_{rr}(r, t)dr^2 + r^2 d\Omega_2^2. \quad (5)$$

Here $d\Omega_2$ is the line element on S^2 with unit radius, t is a Euclidean time variable and r a radial coordinate in three dimensions.

When the derivative $a'(0) = 0$, it turns out that at a time-instant $t = 0$ a black hole appears with a Euclidean de Sitter (EdS) interior. It is interesting to also consider possibilities in which $a'(\eta)$ near the origin is non-zero but relatively small. Thus we are led to properties similar to ‘regular black holes’ (for the latter see e.g. [46] and references therein).

Allowing also for a quantum mechanical ‘vacuum condensate’ [47–52], it makes sense to assume that the Einstein equations hold in the effective sense. This gives the form of the energy-momentum tensor of the condensate, T^μ_ν ,

$$G^\mu_\nu = 8\pi G_N T^\mu_\nu, \quad G^\mu_\nu = R^\mu_\nu - \frac{1}{2} R \delta^\mu_\nu, \quad (6)$$

where G_N is a renormalized Newton constant. For the calculation the software OGRE [53] is very helpful.

The collapsed phase has been judged as being unphysical, presumably because of its singular vertices and its Hausdorff dimensions substantially larger than four. The occurrence of singular vertices has been well explained in terms of ‘balls-in-boxes’ models (cf. [54, 55] and references therein). Here they are interpreted physically as suggesting the presences of black holes or similar objects. A precise comparison of locations cannot be made because the available numerical data has been volume-averaged, blurring locations.

Hausdorff dimensions (local and global) have been estimated [7, 10, 12, 24] from the behavior of volume-volume and volume-distance correlators. The latter were used in [42] to construct effective *metrics* at short distances in *four* dimensions. When they have hyperbolic features, sampling them at discrete distances will easily produce values of local Hausdorff dimension observables that are larger than four. We see no need of these for a characterization of the crumpled phase.

Global Hausdorff dimensions involve scaling at increasing volume, which may be accompanied by ‘anomalous dimensions’. Large values $\gg 4$ are found rather deep in the collapsed phase [10], but towards the phase boundary they diminish and become compatible with or close to four [7, 12]. In [42] high-dimensional or even logarithmic scaling was seen in a volume-distance correlator expressed in the lattice geodesic distance. However, observables expressed in so-called ‘continuum’ distances

(introduced in the same reference) may behave differently, since they involve a volume-dependent re-scaling.

The remainder of this article is organised as follows. Section II introduces our numerical results for $a_G(\eta)$ in (4). Data for κ_2 farthest away from the phase transition are chosen for further analysis in terms of a rational fit function. Section III describes our choice of the integration constant c_G . For comparison other possibilities are also mentioned. In section IV we study transformations to the 3+1 D spherical coordinate system (5). A numerically obtained regular transformation is described in subsection IV A. It appears to have a singular limit as $t \rightarrow 0$ which can be obtained analytically from a singular transformation described in subsection IV B. The limiting metric has black hole features shown in section V. The corresponding Einstein tensor is also shown, highlighting energy density and pressure of the condensate.

Section VI deals with the question: given a regular black hole in the 3+1 spherical coordinate system, what is the result of the inverse transformation to the 4 D spherical system (1)? With the knowledge obtained in section IV this question is answered for a specific example, the Hayward model. Its qualitative properties might be relevant for distinguishing regular from genuine black holes in simulations with larger volumes. Concluding remarks are in section VII.

Appendix A summarises details of the EDT formulation and the volume-distance correlator. In appendix B we show that it can be fitted well by an EdS *metric* at *medium distances*. When expressed in terms of ‘continuum’ distances the fit closely resembles the one in [7]. It is found to have good scaling behavior.

Appendix C is a literal rendition of section 3 in the draft [44]. It contains exact expressions for the massless propagator $G(\eta)$ in continuous space with constant negative curvature $-12/r_0^2$ and its exponential fall-off $\propto \exp(-3\eta/r_0) + \dots$ as $\eta \rightarrow \infty$. Numerical results are presented for the lattice $G(\eta)$ fitted by the exponential form $a \exp(-m\eta) + c$. However, further analysis in appendix D leads to the conclusion that the interpretation $m = 3/r_0$ with r_0 a hyperbolic curvature radius is inappropriate and misleading. (This does not affect the fact that the exponential fit also considered in section II describes the $a_G(\eta)$ data well in a limited fit domain.)

Appendices E and F contain technical details of the coordinate transformation.

II. METRIC SCALE FACTOR FROM MEASURED PROPAGATOR

With the propagators $G(\eta)$ from the numerical simulation described in appendix C the relation (3) can be used to obtain an average metric scale factor as ‘seen’ by the propagator, by treating (3) as a differential equation for $a(\eta)$:

$$3 \partial_\eta \ln[a(\eta)] = -\partial_\eta \ln[-\partial_\eta G(\eta)]. \quad (7)$$

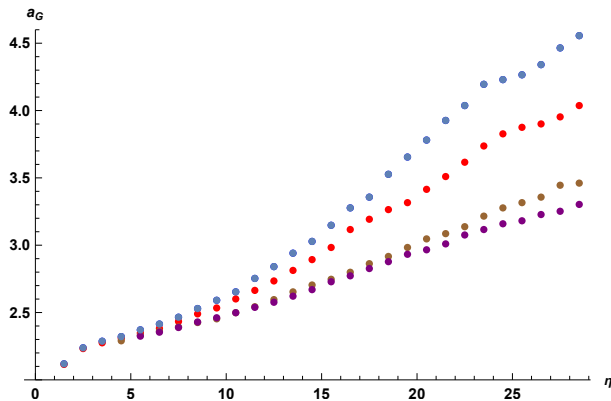


FIG. 1. Lattice $a_G(\eta)$, top to bottom $\kappa_2 = 1.240, 1.245, 1.250, 1.252$; $N_4 = 32k$.

The solutions for $a(\eta)$,

$$a(\eta) \propto \left[-\frac{1}{\partial_\eta G(\eta)} \right]^{1/3}, \quad (8)$$

have a multiplicative integration constant. On the lattice we implement the discrete derivative as

$$G'(\eta + 1/2) = G(\eta + 1) - G(\eta), \quad (9)$$

and define a lattice version of the scale factor by

$$a_G(\eta) = \left[-\frac{1}{G'(\eta)} \right]^{1/3}. \quad (10)$$

The scale factor to represent the average geometry in the continuum contains the multiplicative integration constant c_G ,

$$a(\eta) = c_G a_G(\eta). \quad (11)$$

Results are available for $\kappa_2 = 1.240, 1.245, 1.250$ and 1.252 at $N_4 = 32k$. Figure 1 shows $a_G(\eta)$ for these κ_2 . Unfortunately, we have no information about statistical errors of the retrieved data.

In this study of the collapsed phase it is important that κ_2 is sufficiently far from the phase transition. Judging from the broad susceptibility peak in figure 14 of [42], this holds for $\kappa_2 = 1.240$, and to a lesser extent for $\kappa_2 = 1.245$ which appears located at the edge of the peak (its maximum is at $\kappa_2^c = 1.257$). But the two larger κ_2 have penetrated the susceptibility peak and indeed, their points plotted in figure 1 appear separated from the two lower κ_2 . In the following we concentrate primarily on case $\kappa_2 = 1.240$.

The first three data points at $\eta = 1.5, 2.5$ and 3.5 , where all κ_2 data merge visually, are presumably strongly subjected to lattice artefacts; discarding these, a mental extrapolation to $\eta = 0$ suggests a non-zero $a_G(0) \approx 2.2$.

The pennant-like feature of the last five data points ($\eta \geq 24.5$) is present in both $\kappa_2 = 1.240$ and 1.245

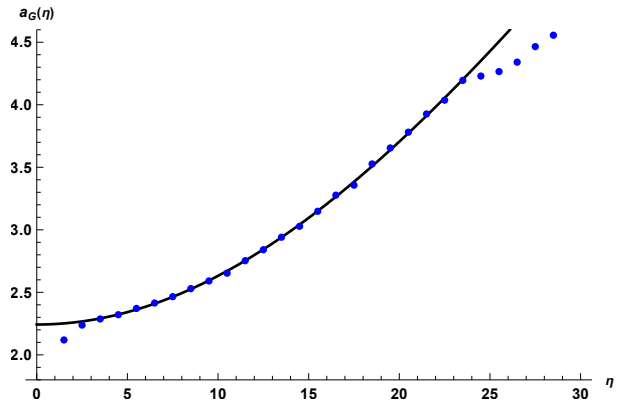


FIG. 2. Lattice $a_G(\eta)$ data (blue dots) and fit function $f_{\text{rat}}(\eta)$ (black curve); $N_4 = 32k$, $\kappa_2 = 1.240$.

which suggests that it is not due to statistical fluctuations. It may indicate a drop in the contributing volume near $\eta = 25$ and also a change in the character of contributing geometries. At large distances, $\eta \gtrsim 25$, we expect branched polymers to dominate the contributions to $a_G(\eta)$ (cf. appendix A).

A good choice of fit function and fit domain appears to be given by

$$f_{\text{rat}}(\eta) = \frac{p_0 + p_1 \eta^2}{1 + q_1 \eta^2}, \quad \eta = \{5.5, 6.5, \dots, 23.5\}. \quad (12)$$

It does significantly better than a mere quadratic fit $p_0 + p_1 \eta^2$ in the region $\eta \geq 19.5$, and even in $\eta \leq 7.5$. The fitted parameters for the smaller two κ_2 are given by

κ_2	p_0	p_1	q_1	$p_1/p_0 - q_1$
1.240	2.24	0.00447	0.000219	0.0018
1.245	2.23	0.00497	0.000616	0.0016

(13)

Figure 2 shows the fit for the κ_2 furthest from the phase transition.

For analytic treatment the simple form

$$f_{\text{ch}}(\eta) = c_{\text{ch}} \cosh(\eta/r_0) \quad (14)$$

is useful for suggesting the form of coordinate transformations in section IV B. Qualitatively $f_{\text{ch}}(\eta)$ is similar to $f_{\text{rat}}(\eta)$ in the fit domain and it approaches asymptotically a Euclidean Anti-de Sitter (EAdS) scale factor with length scale r_0 . However, here r_0 monitors behavior of the data up to medium distances only. For $\kappa_2 = 1.240$ and the same fit domain as in (12) its two parameters come out as $c_{\text{ch}} = 2.32$, $r_0 = 22$.

For discussion we also show a log-plot in figure 3 of $a_G(\eta)$ fitted by an exponential $f_e(\eta) = \exp(e_0 + e_1 \eta)$ in the domain $\eta \in \{9.5, \dots, 24.5\}$. Because of the difference in fit domain the coefficients $e_{0,1}$ differ somewhat from the ones implied by the exponential fit made already for the $G(\eta)$ data in D1.

Of particular interest to our subsequent analysis turns out to be the region near the origin $\eta = 0$. To avoid

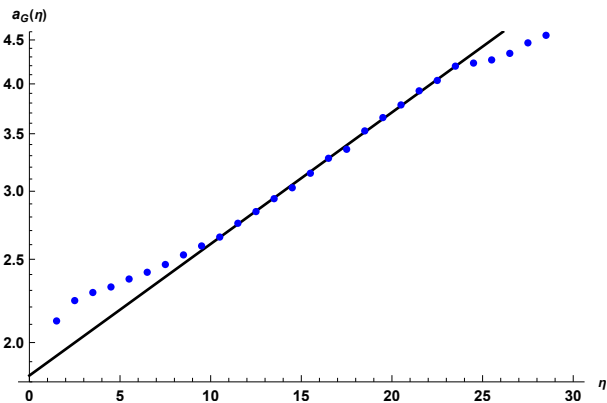


FIG. 3. Log-plot of $a_G(\eta)$ data (dots) and fit function $f_e(\eta) = \exp(e_0 + e_1\eta)$ (black line); $\{e_0, e_1\} = \{0.605, 0.0353\}$; $N_4 = 32k$, $\kappa_2 = 1.240$.

strong lattice artefacts and variable dimension effects we should reach this region by extrapolation from $\eta \gtrsim 6$ towards zero. In the following we *define* the new metric through its fit function, including extrapolation to the origin, and choose the rational function:

$$a_G(\eta) = f_{\text{rat}}(\eta) \quad (15)$$

(keeping in mind that values $\eta > 23.5$ are rather uncertain). It follows the trend of the data from $\eta \simeq 10$ towards the origin better than $f_e(\eta)$, and should therefore also express better possible physics in the data. The fact that the derivative $f'_{\text{rat}}(\eta)$ vanishes at the origin is relevant, we come back to this aspect in the Conclusions section VII.

III. DETERMINATION OF THE INTEGRATION CONSTANT

The metric scale factor $a(\eta) = c_G a_G(\eta)$ is completed by specifying the integration constant c_G . According to $a(\eta)$, the volume within distance η from the origin is

$$V_G(\eta) = 2\pi^2 c_G^3 \int_0^\eta d\bar{\eta} a_G(\bar{\eta})^3. \quad (16)$$

This can be compared with the four-volume in a ball within distance η from the origin as given by the volume-distance correlator, $V(\eta) = N(\eta) v_4$. The question is, at which distance. Medium distances are favoured here since $V(r)$ shows EdS scaling at medium distances (cf. appendix B) and is assumed to have physical significance in this region. This scaling, based on $V'(\eta)$, is subtle and involves a factor λ between lattice distances and distances dubbed ‘continuum’. However, integrated volumes are to be compared directly (cf. (B5), (B6)). An η -dependent $c_G(\eta)$,

$$c_G(\eta) = \left[\frac{N(\eta) v_4}{2\pi^2 \int_0^\eta d\bar{\eta} a_G(\bar{\eta})^3} \right]_{a_G(\bar{\eta}) \rightarrow f_{\text{rat}}(\bar{\eta})}^{1/3}, \quad (17)$$

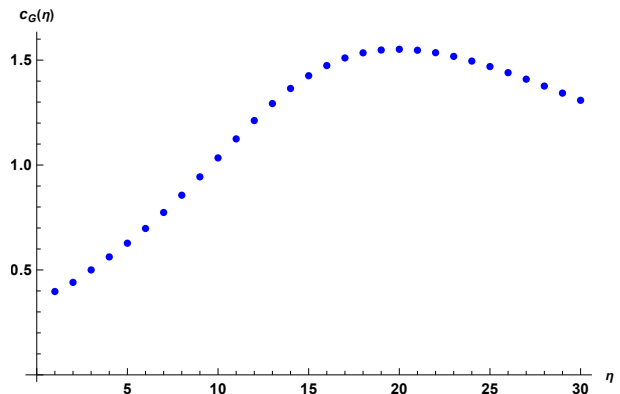


FIG. 4. $c_G(\eta)$ in (17); $N_4 = 32k$, $\kappa_2 = 1.240$.

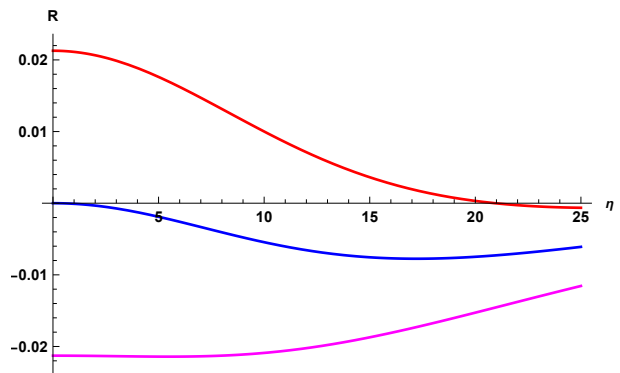


FIG. 5. Curvatures $R(\eta)$ for various c_G . Upper curve (red): $c_G = c_{GS} = 5.3$; middle curve (blue): $c_G = c_{G0} = 7.5$; lower curve (magenta): $c_G = \infty$.

is shown figure 4.

It has a maximum the upper edge of the medium distance region, $\eta \simeq 20$. By a ‘principle of minimal sensitivity’ we choose c_G equal to the value at this point,

$$c_G = c_G(20) = 1.55. \quad (18)$$

A similar value results from the following reasoning: We wish to avoid the region where branched-polymer ‘hair’ contributions dominate over that of a ‘blob’. This is the long distance region which starts at $\eta \simeq 25$. Choosing $\eta = 25$ gives $c_G(25) = 1.46$.

Other values are of interest to see the effect of c_G on various observables, for example the curvature

$$R(\eta) = 6 \left[-\frac{a''(\eta)}{a(\eta)} - \frac{a'(\eta)^2}{a(\eta)^2} + \frac{1}{a(\eta)^2} \right]. \quad (19)$$

With $a(\eta) = c_G f_{\text{rat}}(\eta)$ this becomes a rational function in which numerator and denominator are polynomials of the 4-th degree in η^2 . At the origin it simplifies to

$$R(0) = \frac{6}{c_G^2 p_0^2} - \frac{12 p_1}{p_0} + 12 q_1. \quad (20)$$

Defining c_G such, that R vanishes at the origin leads to

$$c_G = \frac{1}{\sqrt{2} p_0 \sqrt{p_1/p_0 - q_1}} \equiv c_{G0}, \quad (21)$$

and $c_{G0} = 7.5$. A third value of c_G will be considered later in section V when a comparing with the Schwarzschild metric, in (82): $c_{GS} = \sqrt{2} c_{G0} = 5.3$.

The curvatures for c_{G0} and c_{GS} are shown in figure 5. For our fiducial value (18) the curvature is positive and larger than for c_{GS} by an order of magnitude (a factor $\gtrsim 25$ at $\eta = 0$). It is shown in figure 30 together with curvature based on the volume-distance correlator.

IV. TRANSFORMATION TO SPHERICAL COÖRDINATES

We seek to transform the metric (1), more explicitly given by

$$ds^2 = d\eta^2 + a(\eta)^2 d\psi^2 + a(\eta)^2 \sin(\psi)^2 d\Omega_2^2, \quad (22)$$

$$d\Omega_2^2 = d\theta^2 + \sin(\theta)^2 d\phi^2, \quad (23)$$

into the form (5), shown again for convenience,

$$ds^2 = g_{tt}(r, t) dt^2 + 2g_{rt}(r, t) dr dt + g_{rr}(r, t) dr^2 + r^2 d\Omega_2^2. \quad (24)$$

The transformation is specified by a function $y(r, t)$ in

$$r = a(\eta) \sin(\psi), \quad y(r, t) = a(\eta) \cos(\psi), \quad (25)$$

to be determined. In principle

$$0 \leq \eta < \infty, \quad 0 \leq \psi \leq \pi, \quad (26)$$

$$-\infty < t < \infty, \quad 0 \leq r < \infty, \quad (27)$$

in practice $0 \leq \eta \leq \eta_{\max}$ with corresponding limits on r and t depending on $y(r, t)$. Since $a > 0$,

$$y > 0, \quad 0 < \psi < \pi/2, \quad (28)$$

$$y < 0, \quad \pi/2 < \psi < \pi. \quad (29)$$

Note

$$r^2 + y^2 = a^2 \geq h^2, \quad h \equiv a(0), \quad (30)$$

which will be used in the following. We have

$$h \leq a \leq a_{\max}, \quad 0 \leq r \leq r_b \quad (31)$$

where $r_b = a_{\max}$, the maximal r for $y = 0$. With $a_{\max} = a(\eta_{\max}) = c_G a_G(\eta_{\max})$, $\eta_{\max} = 23.5$ (the upper limit of the fit domain), and $c_G \simeq 1.5$ this gives

$$r_b \approx 2h. \quad (32)$$

The case with $a = h$ will be called ‘the boundary equation’.

In the region⁴ where $a(\eta)$ is a monotonously increasing function of η it has a unique inverse $\eta(a)$, and a positive function $F(a)$ can be defined by

$$(da/d\eta)^2 = F(a) = F(\sqrt{r^2 + y^2}). \quad (33)$$

The new metric turns out as

$$g_{tt} = \frac{\dot{y}^2}{r^2 + y^2} \left(\frac{y^2}{F} + r^2 \right), \quad (34)$$

$$g_{rt} = \frac{\dot{y}}{r^2 + y^2} \left(\frac{y(yy' + r)}{F} - r(y - ry') \right), \quad (35)$$

$$g_{rr} = \frac{1}{r^2 + y^2} \left(\frac{(yy' + r)^2}{F} + (y - ry')^2 \right) \quad (36)$$

($\dot{y} = \partial_t y$, $y' = \partial_r y$). We would like y to be such, that the off-diagonal component of the metric vanishes,

$$g_{rt} = 0. \quad (37)$$

Equation (37) can be solved for F to eliminate it from expression (36) for g_{rr} and obtain

$$g_{rr} = 1 - r y' / y, \quad (38)$$

which is useful once y that satisfies (37) is known. Assuming that generically $\dot{y} \neq 0$, solving (37) for y' gives

$$y' = r y \frac{F - 1}{y^2 + r^2 F} \equiv P, \quad P = P(r, y). \quad (39)$$

We also would like y to satisfy the property

$$g_{tt} = 1/g_{rr}, \quad (40)$$

as for the Schwarzschild Euclidean (Anti) de Sitter (SE(A)dS) metrics [56]. Requiring (40) in addition to (37) leads to an equation for y^2 , or

$$\dot{y} = \pm \sqrt{F}. \quad (41)$$

The case with a minus-sign is the time-reversed version of the case with a plus-sign. When using this equation in the following we choose the plus-sign to avoid double covering.

The differential $dy = P dr + \sqrt{F} dt$ is in general *imperfect*, i.e. loosely $\partial_t P \neq \partial_r \sqrt{F}$, meaning

$$\begin{aligned} \partial_y P(r, y) \sqrt{F(\sqrt{r^2 + y^2})} &\neq \partial_r \sqrt{F(\sqrt{r^2 + y^2})} \\ &+ \partial_y \sqrt{F(\sqrt{r^2 + y^2})} P(r, y). \end{aligned} \quad (42)$$

Requiring the differential to be perfect leads to a differential equation for F which is easy to solve,

$$dF/da = 2(F-1)/a \Rightarrow F = 1 + c_F a^2 = 1 + c_F (r^2 + y^2), \quad (43)$$

⁴ This region will include $a \in (h, a_{\max})$.

where c_F is an integration constant. Writing $c_F = \pm 1/r_0^2$ with $r_0 > 0$, the solution of (41⁺) with initial condition $y(r, 0) = 0$ is,

$$y(r, t) = \sqrt{r_0^2 + r^2} \sinh \frac{t}{r_0}, \quad (\text{EAdS}) \quad (44)$$

$$y(r, t) = \sqrt{r_0^2 - r^2} \sin \frac{t}{r_0}, \quad (\text{EdS}) \quad (45)$$

respectively for $c_F > 0$ and $c_F < 0$. In the latter case r is to be limited to $0 < r < r_0$. Upon substitution in (34) – (36) the time-dependence drops out and the diagonal EAdS and EdS metrics emerge,

$$g_{tt}(r) = 1 \pm r^2/r_0^2. \quad (46)$$

Furthermore, treating (33) as a differential equation for the scale factor $a(\eta)$ leads for the + case to the solution $a(\eta) = r_0 \sinh[(\eta - s_0)/r_0]$ with integration constant s_0 (or its η -reversed version), corresponding to hyperbolic space. In the – case it leads to the spherical scale factor $a(\eta) = r_0 \sin[(\eta - s_0)/r_0]$.

Integrating the imperfect differential dy along a path in the (r, t) plane gives a path-dependent result. To avoid this imperfection we shall in section IV A release the condition $g_{tt} = 1/g_{rr}$.

A. Regular transformation to diagonal metric

In this section the condition of diagonality, $g_{rt} = 0$ is kept and the differential equation (39) will be integrated at fixed times. Equation (41) will be used only at one reference r to obtain boundary conditions depending on time for the integration of (39) along r . Then there is no imperfectness of the coordinate transformation.

We concentrate on the fit function (12). It is convenient to rewrite its $a(\eta)$ in the form

$$a(\eta) = h \frac{1 + p\eta^2}{1 + q\eta^2}, \quad h = c_G p_0, \quad p = \frac{p_1}{p_0}, \quad q = q_1. \quad (47)$$

The function $F(a)$ introduced in (33) can be determined via the inverse function $\eta(a)$ of $a(\eta)$; one finds

$$\eta^2 = \frac{a - h}{ph - qa}, \quad a'(\eta)^2 = \frac{4h^2(p - q)^2\eta^2}{(1 + q\eta^2)^4} \quad (48)$$

and

$$F(a) = \frac{4q^3(a - h)(hp/q - a)^3}{h^2(p - q)^2}. \quad (49)$$

The function $F(a)$ is positive between its zeros at $a = h$ and $a = hp/q$ with a maximum at a_{\max} somewhere in between, and only its monotonous branch in $h < a < a_{\max}$ is to be used. In this section results will be shown with $c_G = 1.55$ ($h \simeq 3.3$) (cf. (13) and (18)), for which a_{\max} is only slightly larger than $2h$.

Since an analytical treatment is already awkward in this case and might be prohibitive with more general fit functions, the following is a numerical exploration.

We choose a reference distance r_p and erect a ‘time pole’ $y_p(t; r_p)$ by solving $\dot{y} = \sqrt{F}$ numerically at $r = r_p$:

$$\dot{y}_p(t; r_p) = \sqrt{F\left(\sqrt{r_p^2 + y_p(t; r_p)^2}\right)}, \quad (50)$$

with initial conditions $y = y_0$ at $t = t_0$ chosen as follows. Guided by (44) we assume that $y > 0$ ($y < 0$) when $t > 0$ ($t < 0$). Compatible with this, the initial condition can be taken a minimal $|y|$ at $t = 0$: for $r_p > h$, $y_0 = 0$, for $r_p < h$ the minimal $|y|$ has to comply with the boundary equation in (30):

$$\begin{aligned} y_0 &= 0, & h \leq r_p \leq r_{\max}, & \quad t_0 = 0, \\ &= \pm \sqrt{h^2 - r_p^2}, & 0 \leq r_p \leq h, & \quad t_0 \rightarrow 0^\pm. \end{aligned} \quad (51)$$

The resulting y_p is a monotonically rising function of t . Next, equation (39) implementing $g_{rt} = 0$ is solved (numerically) with a boundary condition attaching y to the pole:

$$y'(r, t; r_p) = P(r, y(r, t; r_p)), \quad y(r_p, t; r_p) = y_p(t; r_p). \quad (52)$$

The solutions $y(r, t; r_p)$ map the (r, t) plane to the (r, y) plane and give a foliation of the latter. The foliation lines do not cross.

Consider erecting a second time pole $\bar{y}_p(\bar{t}; \bar{r}_p)$ at a different position $\bar{r}_p \neq r_p$. This pole will be crossed by a foliation line $y(r, t; r_p)$ of the first pole, $y(\bar{r}_p, t; r_p) = \bar{y}_p(\bar{t}; \bar{r}_p)$, which determines \bar{t} in terms of t . This can be interpreted as a coordinate transformation of the time variable only: $\bar{t} = \bar{t}(t)$. The second pole leads to a second foliation $y(r, \bar{t}; \bar{r}_p)$. However, substituting $\bar{t} = \bar{t}(t)$ will give just the original foliation.

In other words: results of different choices of the pole position are related by coordinate time transformations that depend only on time. We shall see evidence of this in tensor components that transform as a scalar field under such transformations, in particular the spatial components of the metric (which is diagonal in this section) and the diagonal up-down components of the Einstein tensor, $G^\mu_\mu(r, t)$ (no summation).

Results will be shown for two choices of r_p & initial conditions for $y_p(t; r_p)$:

$$r_p = 2h \ \& \ t_0 = 0, \quad y_p(0; 2h) = 0, \quad (53)$$

$$r_p = 0 \ \& \ y_p(t_0; 0) = \pm h(1 + c_t t_0^2), \quad c_t = p - q, \quad (54)$$

with very small but nonzero $c_t t_0^2 > 0$ to get the numerical integration started. (With the indicated choice of c_t , the solution of (50) at small times is $\pm h(1 + c_t t^2 + \mathcal{O}(t^4))$, cf. section IV B.) The case of $-h$ in (54) corresponds to negative t , $y_p(t; r_p)$ and $y(r, t; r_p)$.

Figure 6 shows foliation curves obtained with the two choices of r_p in (53), (54). The curves run over the

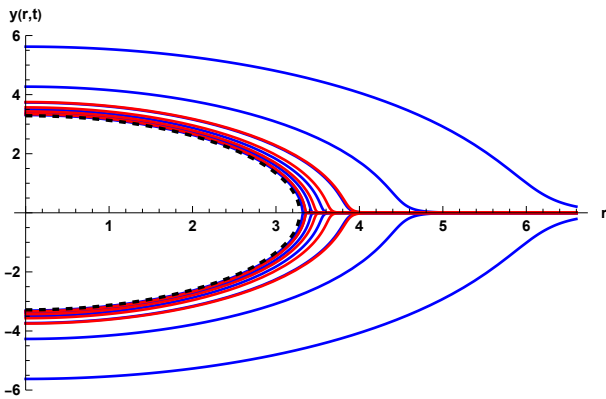


FIG. 6. Foliation curves $y(r, t)$ for $r_p = 2h$ and $t = \pm 10^{k-24}$, $k = 0, 4, 8, \dots, 24$ (blue), and for $r_p = 0$ at times $t = \pm\{3, 5, 7, 9\}$ (red, partially overlaying the blues curves). The inner curve (dashed, black) represents $\pm\sqrt{h^2 - r^2}$; $h = 3.3$.

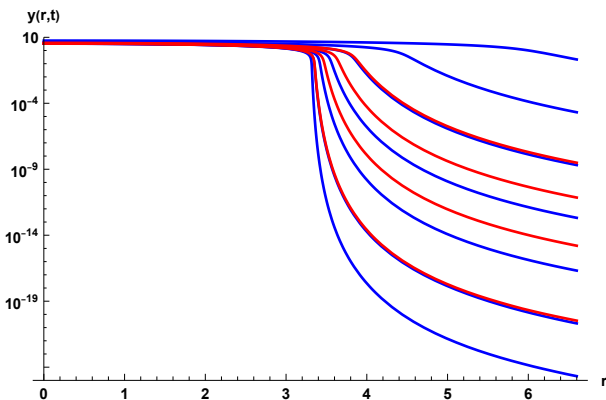


FIG. 7. Logarithmic plot corresponding to the positive y part of figure 6.

whole domain $0 < r < r_{\max}$ and approach the same limit (dashed, black) when $t \rightarrow 0$. Figure 7 shows a corresponding logarithmic plot.

The calculation of the metric needs derivatives of $y(r, t)$. Spatial derivatives can be expressed as functions of y without derivatives using the first equation in (52), repeatedly as needed, for example

$$y'' = \partial_r P(r, y) + \partial_y P(r, y) P(r, y). \quad (55)$$

Time derivatives of y were calculated using nearby foliations at $t \pm \epsilon$ and

$$\begin{aligned} \dot{y}(r, t) &\simeq [y(r, t + \epsilon) - y(r, t - \epsilon)] / (2\epsilon), \\ \ddot{y}(r, t) &\simeq [y(r, t + \epsilon) + y(r, t - \epsilon) - 2y(r, t)] / \epsilon^2, \end{aligned} \quad (56)$$

with small ϵ typically of order $t/10$. (Evaluating y also at $t \pm 2\epsilon$ one can approximate \ddot{y} and also improve the above approximations. The first derivative \dot{y} is needed for g_{tt} , but it turns out that the time derivatives cancel out of components of the Einstein tensor.)

Figure 8 shows $1/g_{rr}(r, t)$ obtained with the help of (38). As t approaches zero an envelope develops, which is

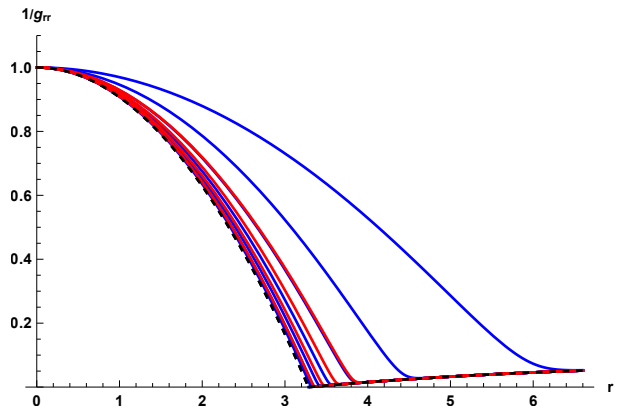


FIG. 8. Plot of $1/g_{rr}$. The dashed (black) curves represent $F(r)$ in the exterior and $1 - r^2/h^2$ in the interior.

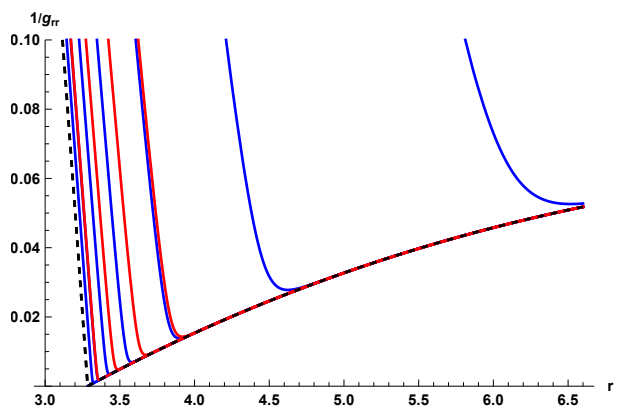


FIG. 9. Closeup of figure 8. The envelope covers visually the $1/g_{rr}$ curves in the exterior region; it is zero at $r = h$.

represented by the dashed black curves. Figure 9 shows a closeup. The envelope is $F(r)$ in the exterior region $r > h$ and switches to $1 - r^2/h^2$ in the interior. In the exterior this can be understood from taking the limit $y \rightarrow 0$ and $y' \rightarrow 0$ in the basic form (36) for g_{rr} . In the interior the limit $y \rightarrow \pm\sqrt{h^2 - r^2}$ leads to $F(h)$ in the denominator in (36) and one has to heed the fact that $F(h) = 0$ (cf. section IV B).

The time component of the metric, g_{tt} calculated from (34) differs very much from $1/g_{rr}$ as shown in figures 10 and 11, note the vertical scale in the latter. The non-invariance of g_{tt} under transformations of the time variable, $t \rightarrow \bar{t}(t)$, has drastic effects here.

For the calculation of the components of the Einstein tensor the expressions given in Exercise 14.16 of [57] can be used; transformed to the Euclidean case they are recorded in appendix E. Figure 12 shows G^t_t with the same conventions as in figures 6 and following. It illustrates that $r_p = 0$ and $r_p = 2h$ give indeed the same G^t_t curves as expected from the scalar nature of $G^t_t(r, t)$ under transformations $t \rightarrow \bar{t}(t)$. An envelope develops as $t \rightarrow 0$ which has a discontinuous jump at $r = h$. Figure 13 shows similar phenomena in G^r_r . For G^θ_θ in figure 14

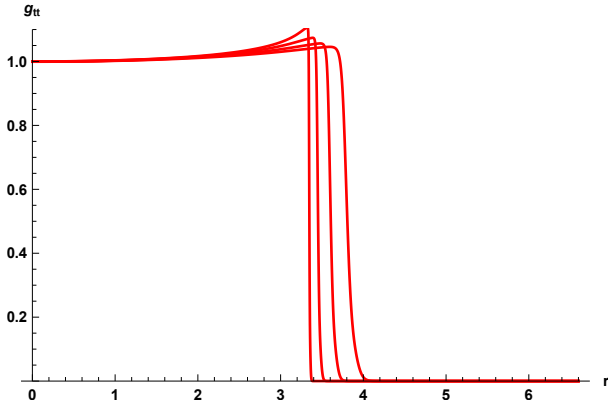


FIG. 10. Time component $g_{tt}(r, t)$ for $r_p = 0$. Left to right in $3.3 < r < 4$: $t = 3, 5, 7, 9$.

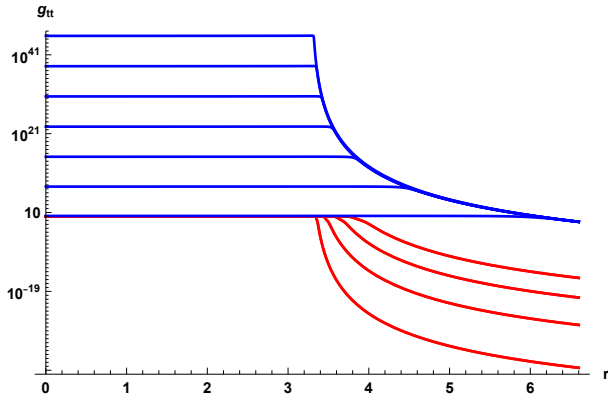


FIG. 11. Log-plot of $g_{tt}(r, t)$. The lower (red) curves correspond again to $r_p = 0$, the upper (blue) curves to $r_p = 2h$.

the envelope is continuous ($G_{\phi}^{\phi} = G_{\theta}^{\theta}$).

The Einstein tensor has an off-diagonal component G_r^t shown in figure 15, which vanishes in the limit $t \rightarrow 0$ for $r \neq h$ and, as argued in appendix F, also at $r = h$ when interpreted in the distributional sense.

The curvature R provides a check on the calculations. The trace of the Einstein tensor is $-R$. Calculating $R = 6(-a''/a - a'^2/a^2 + 1/a^2)$ from the metric (1), which is a function of η^2 , using $\eta^2(a)$ in (48) with $a = \sqrt{r^2 + y^2}$ and the numerically calculated $y(r, t)$ to transform it to (r, t) variables, we can compare it with $-G_{\mu}^{\mu}(r, t)$. The two R match accurately with a point-wise precision of order 10^{-14} % (using Mathematica with default working conditions). This is surprising, since one expects from (56) that the time derivatives of y will have only order percent accuracy. The reason is that \dot{y} and \ddot{y} cancel out of the Einstein tensor, cf. appendix E. The shape of G_{μ}^{μ} is similar to that of G_{θ}^{θ} .

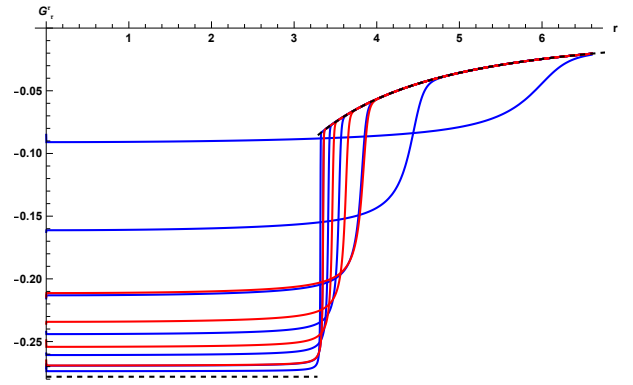


FIG. 12. G_r^t . Upper curves (blue) in $r < h$ correspond to $r_p = 2h$, the curves occasionally joining (red) correspond to $r_p = 0$. The black-dashed lines represent (73), (75).

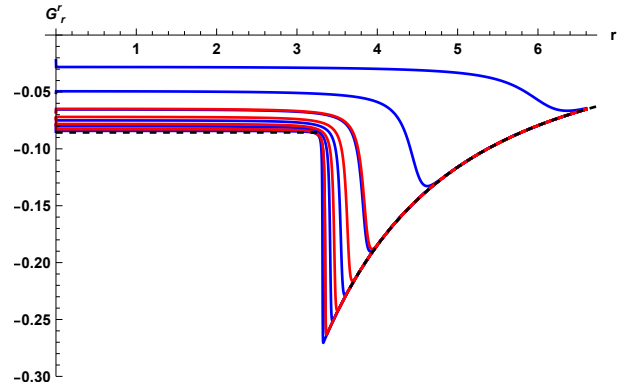


FIG. 13. G_r^r . The black-dashed lines represent (74), (76).

B. Singular transformation implementing $g_{tt} = g^{rr}$ at $t = 0$

The numerical integration of $y' = P$ in section IV A yielded diagonal metrics with spatial inverse components $1/g_{rr} = g^{rr}$ that approached a robust envelope when $t \rightarrow 0$. On the contrary, the magnitude of the component g_{tt} was highly sensitive to differing choices of boundary

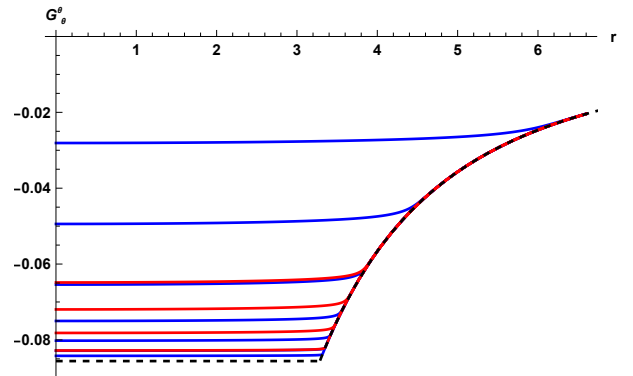
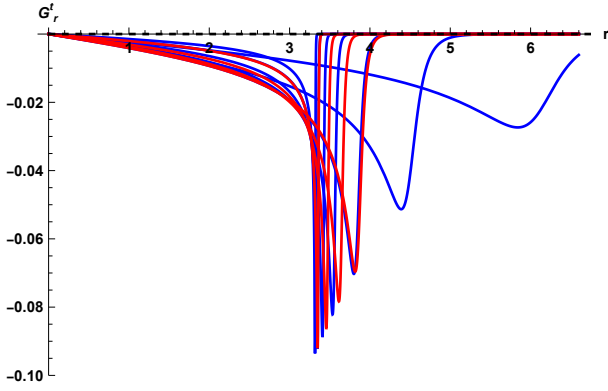


FIG. 14. G_{θ}^{θ} . The black-dashed lines represent (73), (76).

FIG. 15. G^t_r .

conditions (the two pole choices) and the shape of $g_{tt}(r, t)$ differed from $g^{rr}(r, t)$.

In this section we seek to obtain $g_{tt} = g^{rr}$ in the limit $t \rightarrow 0$. We give up diagonality of the metric for general times but seek to recover it at zero time. Consider erecting a pole as in the previous section but here at every $r \in (0, r_{\max})$. We wish to solve $\dot{y} = \sqrt{F}$ analytically at small times and try $y(r, t) = y_p(t; r)$. It is helpful to take a brief look at the solution of this equation in case of the cosh-model,

$$a(\eta) = h \cosh(\eta/r_0), \quad (57)$$

which is simpler to solve than the rat-model. (We recall that here r_0 is meant to parametrize primarily the small to intermediate distance region, $1/r_0^2$ may be thought to represent $2(p - q)$ of the rat-model to $\mathcal{O}(\eta^2)$.) With $a'(\eta)^2 = (h^2/r_0^2)(\cosh^2(\eta/r_0^2) - 1)$ the function F in (33) turns out as

$$F(\sqrt{r^2 + y^2}) = (r^2 + y^2 - h^2)/r_0^2. \quad (58)$$

The solution of (41⁺) with initial condition (51)| $_{r_p \rightarrow r}$ is

$$\begin{aligned} y(r, t) &= \pm \sqrt{h^2 - r^2} \cosh(t/r_0), \quad 0 < r < h, \quad t \gtrless 0, \\ &= \sqrt{r^2 - h^2} \sinh(t/r_0), \quad r > h. \end{aligned} \quad (59)$$

At $t = 0$ this solution satisfies $y' = P$ (trivially in the exterior as $0 = 0$), and the resulting metric becomes indeed diagonal, $g_{rt} = 0$, with

$$\begin{aligned} g_{tt}(r, 0) = 1/g_{rr}(r, 0) &= 1 - r^2/h^2, \quad r < h, \quad (60) \\ &= (r^2 - h^2)/r_0^2 = F(r), \quad r > h. \end{aligned}$$

Generalizing to other models, e.g. the rat-model, consider a factorized form as suggested by (59) in the exterior,

$$y(r, t) = u(r) t. \quad (61)$$

Equation (35) shows that it leads to a vanishing off-diagonal component at $t = 0$, $g_{rt}(r, 0) = 0$, independent of $u(r)$. (The equation $y' = P$ is again solved trivially as $0 = 0$.) Furthermore (36) gives

$$g_{rr}(r, t) = \frac{1}{F(r)} + \mathcal{O}(t^2), \quad (62)$$

also independent of $u(r)$, whereas (34) gives

$$g_{tt}(r, t) = u(r)^2 + \mathcal{O}(t^2). \quad (63)$$

Hence, requiring $g_{tt}(r, 0) g_{rr}(r, 0) = 1$ we get

$$u(r) = \sqrt{F(r)}. \quad (64)$$

and the equation $\dot{y} = \sqrt{F}$ is indeed satisfied at $t = 0$.

In the interior the Ansatz is,

$$y(r, t) = \pm \sqrt{h^2 - r^2} (1 + c_t t^2), \quad t \gtrless 0, \quad (65)$$

which has a time-dependence similar to that of the cosh-model for small t (cf. first line in (59)). Since $F[h] = a'(0)^2 = 0$ (cf. (33)), F vanishes in the interior at $t = 0$:

$$F(\sqrt{r^2 + y(r, 0)^2}) = F[h] = 0. \quad (66)$$

Its expansion in t starts out as

$$F(\sqrt{r^2 + y(r, t)^2}) = (h - r^2/h) F'(h) c_t t^2 + \mathcal{O}(t^4). \quad (67)$$

The equation $y' = P$ is satisfied at $t = 0$. When $t \rightarrow 0$, the off-diagonal part of the metric g_{rt} in (35) contains $1/F$ which blows up, and it contains \dot{y} which vanishes. Working out the details we find

$$g_{rt} = -2r \left(1 + \frac{2}{hF'(h)} \right) c_t t + \mathcal{O}(t^3). \quad (68)$$

Hence, the interior metric becomes also diagonal at time zero. Furthermore, after some algebra:

$$g_{rr}(r, t) = \frac{h^2}{h^2 - r^2} + \mathcal{O}(t^2), \quad (69)$$

$$g_{tt}(r, t) = \frac{h^2 - r^2}{h^2} \frac{2h c_t}{F'(h)} + \mathcal{O}(t^2). \quad (70)$$

Requiring $g_{tt}(r, 0) g_{rr}(r, 0) = 1$ determines c_t ,

$$c_t = \frac{F'(h)}{2h}, \quad (71)$$

and with this choice the equation $\dot{y} = \sqrt{F}$ is indeed solved to leading order in t . For the rat-model this becomes

$$c_t = p - q, \quad (72)$$

which was used in section IV A for the case $r_p = 0$.

The metric component $g_{tt}(r, 0)$ following from (49), (63), (64), (69) – (71), is shown in figures 8 and 9 by the dashed black curves.

The Einstein tensor G^μ_ν contains time derivatives of the metric which is non-diagonal at non-zero t and a little complicated. For the daunting task of its calculation the software OGRE [53] is very helpful. The results in the limit $t \rightarrow 0$ are fairly simple, $G^\mu_\nu(r, 0)$ is diagonal and in the exterior region, $r > h$:

$$G^t_t = G^\theta_\theta = G^\phi_\phi = -\frac{1}{r^2} \left[1 + \frac{4(hp - qr)^2(h^2p - 2h(p + 2q)r + 5qr^2)}{h^2(p - q)^2} \right], \quad (73)$$

$$G^r_r = -\frac{3}{r^2} \left[1 + \frac{4(h - r)(hp - qr)^3}{h^2(p - q)^2} \right]. \quad (74)$$

In the interior region $0 < r < h$:

$$G^t_t = -\frac{3}{h^2}, \quad (75)$$

$$G^r_r = G^\phi_\phi = G^\theta_\theta = -\frac{1}{h^2} + 4(p - q). \quad (76)$$

These limit forms are shown in figures 12 – 15 by the black dashed curves. Note that G^t_t and G^r_r are discontinuous at $r = h$, but not G^θ_θ .

Figures 6 – 15 suggest strongly that the limit $t \rightarrow 0$ of $y(r, t)$, $g_{rr}(r, t)$ and $G^\mu_\nu(r, t)$ in the regular coordinate transformation is given by the $t = 0$ results of the singular transformation; we assume this to be true.

V. BLACK HOLE FEATURES

In the previous sections we studied a regular coordinate transformation and a singular one, which led to the same results in the limit $t \rightarrow 0$ for the Einstein tensor and for the non-temporal components of the metric. Furthermore, the singular transformation could be tuned such that:

$$g_{tt}(r, 0) = 1/g_{rr}(r, 0), \quad (77)$$

$$1/g_{rr} = F(r), \quad h < r < r_b, \quad (78)$$

$$= 1 - r^2/h^2, \quad 0 < r < h, \quad (79)$$

$$g_{tr}(r, 0) = 0 \quad (80)$$

(Note $r_b \approx 2h$). This metric describes at $t = 0$ a black-hole with horizon radius $r = h$ and surface gravities κ_\pm :

$$2\kappa_+ = \lim_{r \rightarrow h^+} \partial_r g_{tt}(r, 0) = F'(h) = 4h(p - q),$$

$$2\kappa_- = \lim_{r \rightarrow h^-} \partial_r g_{tt}(r, 0) = -\frac{2}{h}. \quad (81)$$

The interior region $0 < r < h$ is like an EdS space.

For a Euclidean Schwarzschild black hole with horizon radius r_S and $r > r_S$, $g_{tt}(r) = 1 - r_S/r$, the surface gravity $\kappa_S = 1/(2r_S)$ [58]. Our choice for the integration constant c_G was made by comparison of volumes as described in section III, but it is interesting to see what choice of c_G follows from matching the horizon radius $h = r_S$ with the surface gravity $\kappa_+ = \kappa_S$: this gives

$$c_G = \frac{1}{2p_0\sqrt{p - q}} \equiv c_{GS}. \quad (82)$$

With the fitted parameter values (13) $c_{GS} = 5.3$ and $h \simeq 12$, for $\kappa_2 = 1.240$.

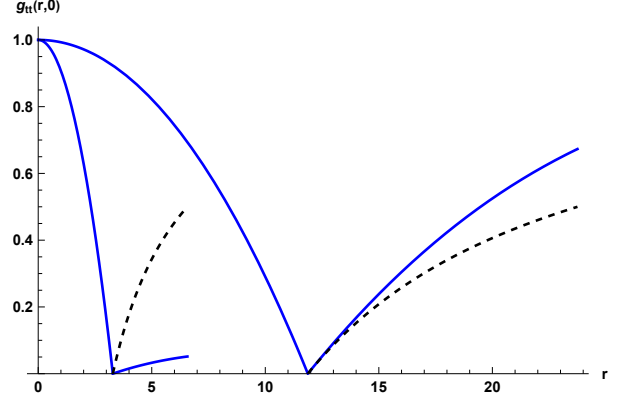


FIG. 16. Metric component $g_{tt}(r, 0)$ for $c_G = 1.46$ ($h = 3.3$) and $c_G = c_{GS} = 5.3$ ($h = 11.9$), $\kappa_2 = 1.240$. Corresponding Schwarzschild metrics are also shown (black, dashed).

Figure 16 shows $g_{tt}(r, 0)$ for two values of c_G , together with the Schwarzschild metric (dashed). The second derivative of $g_{tt}(r, 0)$ at the horizon is independent of c_G and given by

$$F''(h) = -24q_1. \quad (83)$$

Its negative sign ($-q_1 < 0$) matches the concavity of g_{tt} in $r > h$, which it shares with the Schwarzschild form. (With the fit function $f_{ch}(\eta)$ the g_{tt} curve has the wrong convex behavior.)

Assuming the Einstein equations to be valid in the effective sense, the condensate energy and pressure are given by the Einstein tensor, as in (6). When $t \rightarrow 0$ it becomes diagonal with energy density and pressures given by

$$8\pi G_N \{\rho, p_r, p_\theta, p_\phi\} = \{-G^t_t, G^r_r, G^\theta_\theta, G^\phi_\phi\}. \quad (84)$$

The interior energy-density ρ is positive and the pressure p is negative for $c_G < c_{GS}$, as shown in figure 17. Figure 18 shows the case $c_G = c_{GS}$, for which the interior pressure vanishes (note the difference in scale). For the case $c_G = c_{G0}$ in (21) the interior pressure is positive, as shown in figure 19. In this case the curvature $R = -\sum_\mu G^\mu_\mu(r, 0)$ vanishes in the interior and is continuous at $r = h$.

Discontinuities at $r = h$ may be expected from the discontinuous first derivative of $g_{tt}(r, 0)$ at $r = h$, as evident in figure 16 and the different surface gravities κ_\pm in (81). The Einstein tensor contains two derivatives of the metric and when these are both spatial a Dirac delta distribution may also be present. Using the Heaviside

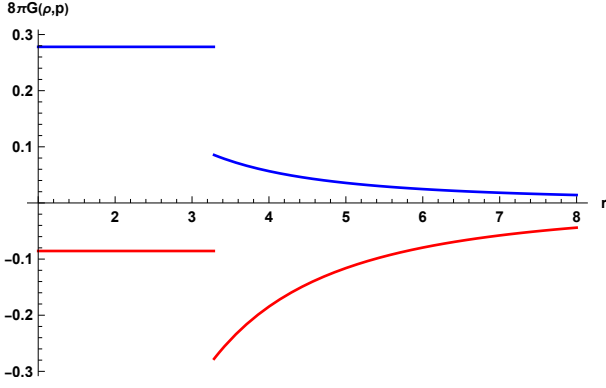


FIG. 17. Energy density $8\pi G_N \rho$ (blue, positive) and pressure $8\pi G_N p_r$ (red, negative) for $c_G = 1.46$ ($h = 3.3$).

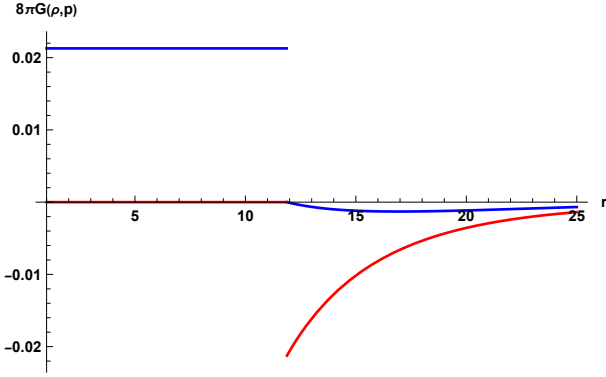


FIG. 18. As in figure 17 for $c_G = c_{GS}$ in (82), $c_G = 5.3$ ($h = 12$). In this case the pressure vanishes in the interior $r < h$.

step function $\theta(x)$, $d\theta(x)/dx = \delta(x)$, $x\delta(x) = 0$, and the expressions in problems 14.13 or 14.16 of [57], equations (77) – (81) lead to a contribution to the transverse pressure $p_\theta = p_\phi$,

$$\Delta p_\phi = \frac{1}{8\pi G_N} \partial_r^2 [(\kappa_+ \theta(r-h) + \kappa_- \theta(h-r))]$$

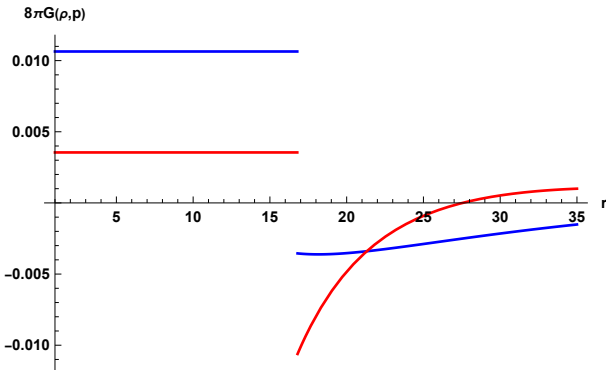


FIG. 19. Energy density (blue) and pressure (red) as in figure 17 for $c_G = c_{G0} = 7.5$ ($h = 17$) in (21).

$$= \frac{\Delta\kappa}{8\pi G_N} \delta(r-h), \quad \Delta\kappa = \kappa_+ - \kappa_- > 0. \quad (85)$$

On the other hand, one would expect the curvature invariant $R(r)$ to be continuous at the horizon; R is equal to minus the trace of the Einstein tensor, and indeed continuous at $r = h$ by (73)–(76). Since $R = 8\pi G_N(\rho - p_r - p_\theta - p_\phi)$, this would imply a contribution to the energy density

$$\Delta\rho = \frac{\Delta\kappa}{4\pi G_N} \delta(r-h) \quad (86)$$

which cancels $\Delta p_\theta + \Delta p_\phi$ in R . Integrated over the horizon this can be interpreted as a boundary layer surface tension [51].

However, if so, then one expects some regulated version of the Dirac distribution blowing up at small diminishing t . But there is no sign of this in figure 14. Indeed, as shown in appendices E and F, such developing singular behavior is canceled exactly by a similar contribution with two time derivatives of the metric. After all cancellations are taken into account the Einstein tensor can be expressed in a form that depends explicitly only on r , y , F and its first derivative F' , but not anymore on derivatives with respect to r and t , cf. (E17) – (E20). These formulas apply equally well to section IV A as here and it seems remarkable that the envelope in figure 14 is described correctly by the consequences of (61) and (65). Thus, *no evidence emerges* as $t \rightarrow 0$ for a boundary layer surface tension as in [51].

The integrated Misner-Sharp mass at $t = 0$ is by (84) and (75),

$$\lim_{r \rightarrow h^-} 4\pi \int_0^r d\bar{r} r^2 \rho = \frac{h}{2G_N} \equiv M. \quad (87)$$

The mass (87) has the Schwarzschild form. The binding-energy estimate made in [38] was $\sqrt{G_N} \approx 8$ (for $\kappa_2 = 1.255$). Taking $\sqrt{G_N} = 10$ gives an idea of the order of magnitude of M in Planck units, for our fiducial case $c_G \simeq 1.5$, $h \simeq 3.3$: $M\sqrt{G_N} \approx 0.2$.

VI. TRANSFORMING THE HAYWARD MODEL

The time-independence of the static version of Hayward's model [59] allows a simple transformation to imaginary time, resulting in the Euclidean model:

$$ds^2 = f(r) dt^2 + \frac{1}{f(r)} dr^2 + r^2 d\Omega_2^2, \quad (88)$$

$$f(r) = 1 - \frac{2mr^2}{2ml^2 + r^3}.$$

The two parameters m and l are positive and have the dimension of length. For small r the metric is like EdS, $f(r) \simeq 1 - r^2/l^2$, and for large r it is 'Newton-like' $f(r) \simeq 1 - 2m/r$. Figure 20 shows $f(r)$ for several values of m at fixed l . With sufficiently large m there are two real zeros

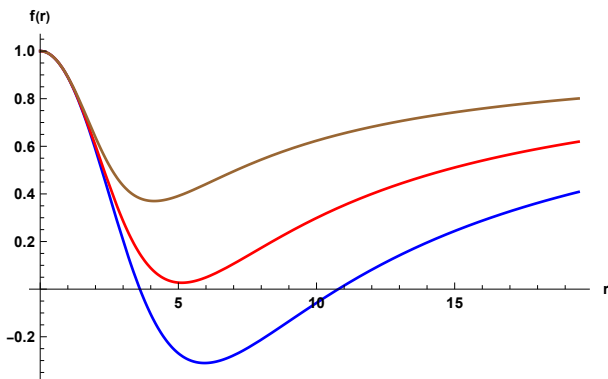


FIG. 20. Hayward function $f(r)$: top to bottom $m = 0.5 m_*$, $0.96 m_*$, $1.5 m_*$ and $l = 3$.

at $r_+ > r_- > 0$, which coincide, $r_+ = r_- = r_*$, when m is reduced to a critical value m_* . Then also $f'(r_*) = 0$, which together with $f(r_*) = 0$ determines

$$m_* = \frac{3\sqrt{3}}{4} l, \quad r_* = \sqrt{3} l. \quad (89)$$

The aim here is to determine the scale factor $a(\eta)$ in an $SO(4)$ invariant metric of the form (1) such that a transformation to spherical coordinates (5) gives the metric (88) in the limit $t \rightarrow 0$. For this purpose the results of the previous sections which led to $g^{rr}(r, 0) = F(r)$ can be used (cf. (61) – (64)). Thus

$$F(r) = f(r), \quad (90)$$

and we can find $a(r)$ from the definition of F in (33), by solving the differential equation

$$a'(\eta) = \sqrt{f(a(\eta))}. \quad (91)$$

Since the Hayward model describes a regular black hole it is natural to fix the integration constant by requiring regularity at the origin,

$$a(0) = 0. \quad (92)$$

To avoid a conical singularity also unit slope $a'(0) = 1$ is required, which is satisfied since $f(0) = 1$.

The small and large η behavior of the solution of (91), (92) are given by

$$\begin{aligned} a(\eta) &\approx l \sin(\eta/l), & a(\eta)^3 &\ll 2ml^2, & (93) \\ &\approx \eta - m \ln(\eta/m) + \text{const}, & a(\eta)^3 &\gg 2ml^2. & (94) \end{aligned}$$

When $m \geq m_*$, the solution of (91), (92) has a fixed point at the first zero of $f(a)$,

$$a(\eta) \rightarrow r_-, \quad \eta \rightarrow \infty, \quad (m \geq m_*). \quad (95)$$

For $m < m_*$ but close to m_* the solution can have a flat region $a(\eta) \approx r_*$ before the asymptotic behavior (94) sets in. Hence r_* is similar to h in the rat-model. However, the surface gravities at r_* vanish, $\kappa_{\pm} = \lim_{r \rightarrow r_*^{\pm}} f'(r)/2 = 0$.

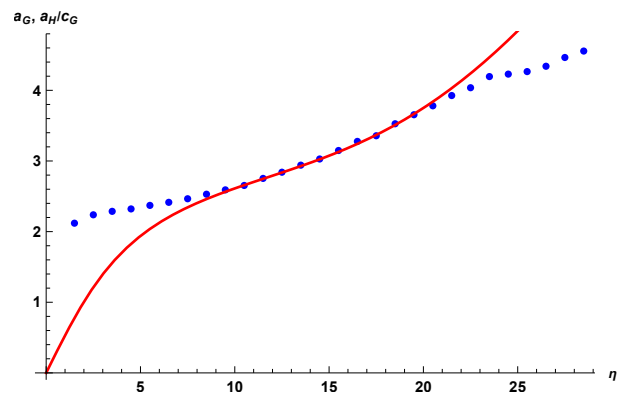


FIG. 21. Data of $a_G(\eta)$ (blue) as in figure 2 matched by $(1/c_G) a(\eta)$, with $1/c_G = 0.54$ and $a(\eta)$ the solution of (91), (92) with $m = 0.96 m_*$, $l = 3$.

A match (by hand and eye) of $(1/c_G) a(\eta)$ to the data in figure 2 is shown Figure 21. Starting from the origin the curve reaches the data at much larger distances than in figure 2. This suggests that such fits may be more appropriate in computations reaching smaller lattice spacings (in physical units). At long distances $a(\eta)$ approaches flat spacetime behavior according to (94) and has to depart from lattice data.

VII. CONCLUSIONS

We explored the construction of an effective metric ‘experienced’ by massless fields in the EDT formulation of quantum gravity. Numerical results were available from a previous study in the collapsed phase. The geometry described by the ‘new metric’ was found to have black hole features.

Further support of a physical interpretation of collapsed phase comes from the scaling study in appendix B of the ‘old metric’ based on the volume-distance correlator at medium distances. The EdS fit in this region has a curvature radius r_{0c} which scales as $r_{0c} \propto N_4^{1/d_s}$ with $d_s \approx 4.3$, or exactly 4 when incorporating a finite-volume correction (figure 31). Using r_{0c} as a scaling length the metric $a_c(\eta_c)$ shows good scaling (figure 35).⁵ The more sensitive local curvature $R_c(\eta_c)$ shows scaling but also deviations (figure 36) which we do not understand; perhaps this observable is too ambitious for the current data, or the scaling sequence $\{N_4, \kappa_2(N_4)\}$ is not optimal.

In our fiducial example $\{N_4, \kappa_2\} = \{32k, 1.24\}$, a fair match at medium distances of the volumes $V_G(\eta)$ and $V(\eta)$ of the new and old metrics,

$$V_G(\eta) = 2\pi^2 c_G^3 \int_0^\eta d\bar{\eta} a_G(\bar{\eta})^3, \quad (96)$$

⁵ Recall η is denoted by r in appendices A, B, C, D.

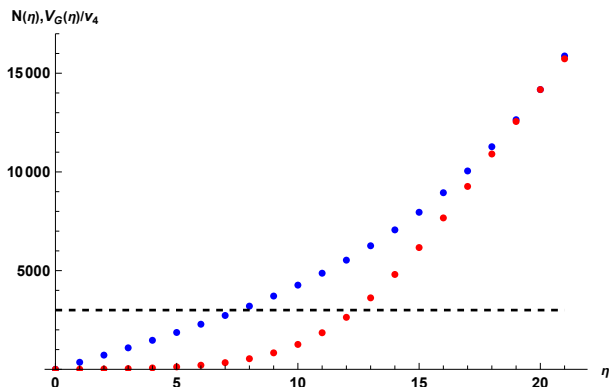


FIG. 22. Comparison of $V_G(\eta)/v_4$ in (97) and $N(\eta)$ with N_{sing} : top to bottom at $r = 10$: $V_G(\eta)/v_4$ (blue), N_{sing} (black dashed), $N(\eta)$ (red); $N_4 = 32k$, $\kappa_2 = 1.240$, $c_G = 1.55$.

$$V(\eta) = N(\eta) v_4, \quad (97)$$

made it possible to determine the integration constant c_G (figure 4). With this value $\simeq 1.5$, curvatures derived from the two metrics acquired similar values at medium distances (figure 30).

The quantum average blurs the position of a singular vertex relative to the origin and the way this works out differs between the two metrics. In our fiducial example there is one singular vertex with an average associated volume (the number of simplices containing it) $N_{\text{sing}} \approx 3000$ (cf. [28], figure 1, $\kappa_0 = 2\kappa_2 = 2.48$). When associating the singular vertex with a black hole ‘detected’ by metric $c_G a_G(\eta)$, $V_G(\eta)$ should reach $N_{\text{sing}} v_4$ at not large η , preferably still in the short distance region. This does indeed happen for $V_G(\eta)$, but not for $V(\eta)$, as shown in figure 22. In the volume-distance correlator the blurring effect seems very strong.

The blurring effect might be diminished by a ‘center of mass’ selection as described in [6]. Otherwise, it seems natural to randomly choose the origin in the singular volume, perhaps averaging over it before taking the quantum average over configurations. This would partially break the discrete remnant of diffeomorphism invariance in DT. The situation appears analogous to spontaneous symmetry breaking in field theory.

The intuitive idea that the collapsed phase with its singular vertices can tell us something about black holes stimulated a change of coordinates that indeed showed black hole-like features, at time zero. We studied the effect of two types of coordinate transformations, a regular one producing a diagonal metric with $g_{tt}(r, t) \neq g^{rr}(r, t)$ at all times and a singular one producing a metric which becomes diagonal only in the limit $t \rightarrow 0$ with $g_{tt}(r, 0) = g^{rr}(r, 0)$. At time zero the component $g^{rr}(r, 0)$ is the same for both transformations. As shown in figure 16 it is zero at $r = h$, as for a black hole with gravitational radius h . The singular transformation has a singularity at this point, which is akin to the transformation between the Schwarzschild-Droste black hole and its Kruskal-Szekeres

extension [60–64].

The numerical study of the regular transformation showed that the left cuspy curve in figure 16 is the limiting envelope of smooth curves representing $g^{rr}(r, t)$ (figure 9). The time component $g_{tt}(r, t)$ differed from $g^{rr}(r, t)$, in shape and, depending on boundary conditions specifying the implementation of the transformation, also by many orders of magnitude. These changes in boundary conditions correspond to transformations $t \rightarrow \bar{t}(t)$ under which $y(r, t)$ and $g^{rr}(r, t)$ behave as scalar fields, but not $g_{tt}(r, t)$ which may suffer large multiplicative factors. Diagonal mixed components of the Einstein tensor, $G^\mu_\nu(r, t)$, $\mu = \nu$, do also transform as a scalar field under $t \rightarrow \bar{t}(t)$ and they approach the same zero time limit as with the singular transformation (figures 12 – 14). Remarkably, the off-diagonal $G^t_r(r, t)$ also did not suffer from the time ambiguity; it was found to vanish when $t \rightarrow 0$ and evidence was given that this holds also in the distributional sense (figure 15 and appendix F).

A shell-like singular distribution in the transverse pressure $\propto G^\theta_\theta(r, 0)$ at $r = h$ suggests itself as a consequence of the discontinuous first derivative $\lim_{r \rightarrow h^\pm} \partial_r g_{tt}(r, 0)$. But with the regular transformation such a shell is absent due to a remarkable cancellation with a singular contribution to G^θ_θ involving time derivatives (cf. appendix F). One also notes that the local minimum in $g^{rr}(r, t)$ approaches $r = h$ when $t \rightarrow 0$ (figure 9) and the derivative at the minimum remains zero in the limit. A gravastar-like shell [51] is not supported in this study.

The coordinate transformations taught us that the occurrence of a horizon is closely related to the minimal derivative of $a(\eta) = c_G a_G(\eta)$, hence, to the properties of the function $f_{a_G}(\eta)$ used to fit the discrete $a_G(\eta)$ data (cf. (78), (33)). For fit functions in which the derivative $f'_{a_G}(0)$ vanishes, $h = c_G f_{a_G}(0)$ is the horizon radius of a black hole, with interior region the three-sphere with radius h . This appears to be a quite natural possibility, which was incorporated by our choice $f_{a_G}(\eta) = f_{\text{rat}}(\eta)$.

Another possibility is a derivative $f'_{a_G}(\eta)$ that does not vanish at the origin and is very small at some positive η . This was illustrated by applying the inverse coordinate transformation to the Hayward model and matching the result to the $a_G(\eta)$ data at medium distances. More extensive computations are needed to determine which possibility is viable.

The method of obtaining a metric based on the propagation of massless fields may also give a new perspective of EDT’s elongated phase, and the spatial collapsed-elongated boundary region (even at the transition)⁶.

ACKNOWLEDGMENTS

The simulation results presented here were carried out by B.V. de Bakker in 1996 on the IBM SP1 and SP2

⁶ Its first-order nature permits phase-coexistence, cf. [15] figure 8.

at SARA and the Parsytec PowerXplorer and CC/40 at IC3A, work supported in part by FOM (nowadays subdivision of the Netherlands Organization for Scientific Research (NWO)).

I thank the Institute of Physics of the University of Amsterdam for its hospitality and the use of its facilities contributing to this work.

Appendix A: EDT and metric from a volume-distance correlator⁷

The EDT spacetimes used here are piece-wise flat manifolds consisting of equilateral 4-simplexes glued together at their 3-simplex boundaries, called ‘combinatorial triangulations’. The number of i -simplexes in these simplicial complexes is denoted by N_i , $i=1, \dots, 4$. In the present study their topology is S^4 . The volume of an i -simplex is given by

$$v_i = \frac{\ell^i \sqrt{i+1}}{i! \sqrt{2^i}}, \quad (\text{A1})$$

with ℓ the spacing between the lattice points. The centers of the 4-simplexes make up the dual lattice, with spacing $\tilde{\ell} = \ell/\sqrt{10}$. In the following the dual lattice will be important. *Unless other wise indicated we shall be using units $\tilde{\ell} = 1$.*

Let t denote a triangle, $t = 1, \dots, N_2$. The integral of the scalar curvature around a single triangle is given by [65, 66]

$$\int_t d^4x \sqrt{g} R = 2v_2(2\pi - o_t \theta) \equiv R_t, \quad (\text{A2})$$

where $\theta = \arccos(1/4)$ and o_t is the order of the triangle, the number of 4-simplexes containing t . Summing over all triangle contributions gives

$$\int d^4x \sqrt{g} R = \sum_t R_t = 2v_2(2\pi N_2 - 10\theta N_4). \quad (\text{A3})$$

The Einstein-Hilbert action S_{EH} with bare parameters G_{N0} and Λ_0 becomes

$$\frac{1}{16\pi G_{\text{N0}}} \int d^4x \sqrt{g} (2\Lambda_0 - R) = \kappa_4 N_4 - \kappa_2 N_2, \quad (\text{A4})$$

where

$$\kappa_2 = \frac{v_2}{4G_{\text{N0}}}, \quad \kappa_4 = \frac{\Lambda_0 v_4 + 10\theta v_2}{8\pi G_{\text{N0}}}. \quad (\text{A5})$$

The partition functions are sums over triangulations $\mathcal{T}(N_4)$ at fixed topology,

$$Z = \int Dg e^{-S_{\text{EH}}} \rightarrow Z(\kappa_2, \kappa_4), \quad (\text{A6})$$

$$Z(\kappa_2, \kappa_4) = \sum_{N_4} e^{-\kappa_4 N_4} Z(\kappa_2, N_4), \quad (\text{A7})$$

$$Z(\kappa_2, N_4) = \sum_{\mathcal{T}(N_4)} \frac{1}{C(\mathcal{T})} e^{\kappa_2 N_2}, \quad (\text{A8})$$

$$Z(\kappa_2, \beta, N_4) = \sum_{\mathcal{T}(N_4)} \frac{M(\mathcal{T}, \beta)}{C(\mathcal{T})} e^{\kappa_2 N_2}. \quad (\text{A9})$$

Here $C(\mathcal{T})$ is the order of the symmetry group (automorphisms) that \mathcal{T} may have, which is relevant for strong coupling expansions on small lattices [8, 67]. In (A9) a ‘measure term’ [9] is inserted which introduces a third coupling parameter β ,

$$M(\mathcal{T}, \beta) = \prod_t o_t^\beta = \exp \left[\beta \sum_t \ln \left(\frac{2\pi}{\theta} - \frac{R_t}{2\theta v_2} \right) \right], \quad (\text{A10})$$

where we used (A2). It depends logarithmically on the curvature but the product form shows that is still local.

We worked with the fixed-volume, ‘canonical’, partition function (A8), i.e. $\beta = 0$. Then the quantum average of observables O is

$$\langle O \rangle = \frac{1}{Z(\kappa_2, N_4)} \sum_{\mathcal{T}(N_4)} e^{\kappa_2 N_2} O(\mathcal{T}). \quad (\text{A11})$$

In particular, average scalar field propagators on \mathcal{T} were computed by inverting a lattice version of the Laplace-Beltrami operator as in [36]. With S^4 topology this operator has an exact zero mode, the constant mode. Computations of propagators in four dimensions were pioneered in [1].

We call the average number of elementary 4-simplexes at dual lattice distance r from an arbitrary origin the volume-distance correlator, $n(r)$. The average number of simplexes within distance r is

$$N(r) = N(0) + \sum_{\bar{r}=1}^r n(\bar{r}), \quad N(0) = 1, \quad (\text{A12})$$

in terms of which

$$n(r) = N(r) - N(r-1) \equiv N'(r-1/2) \equiv \tilde{n}(r-1/2). \quad (\text{A13})$$

Here N' is a discrete derivative and $\tilde{n}(r)$ is a shifted version of $n(r)$.

These observables have been compared with the volumes (2) of isotropic spaces in the continuum. Typical examples are maximal symmetric spaces, which metrics were matched in [42] to volume-distance correlators at relatively small distances.

Figure 23 shows a collapsed-phase example relevant for the present work. It can be fitted at small distances by the hyperbolic-sine form

$$c r_0^3 \sinh[(r-s)/r_0]^3, \quad (\text{A14})$$

which corresponds to a 4D hyperbolic space with constant negative curvature $-12/r_0^2$, as follows from (19)

⁷ In appendices A, B, C and D, η is denoted by r .

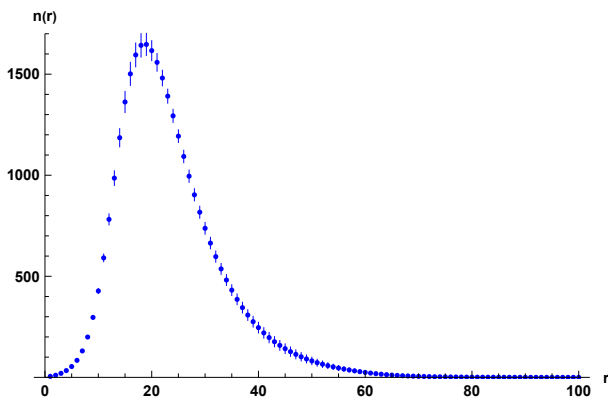


FIG. 23. Volume-distance correlator $n(r)$ for $N_4 = 32000$, $\kappa_2 = 1.240$; jackknife errors.

when $a(r) = r_0 \sinh(r/r_0)$. The largest point in the fit domain, $2 \leq r \leq 10$, is still smaller than the inflexion point of $n(r)$ near $r = 13$. The fitted parameters are

$$c = 0.093, s = -2.7, r_0 = 10.1 \Rightarrow \lambda = 0.324, r_{0c} = 3.28 \quad (\text{A15})$$

(λ and r_{0c} are defined in (A20) and (A21)).

At large distances $n(r)$ can be fitted by a Gaussian form

$$\exp(e_0 - e_1 r - e_2 r^2), \quad (\text{A16})$$

which represents branched-polymer behavior at large r [24, 42]. The fitted parameters are

$$e_0 = 9.05, \quad e_1 = 0.0635, \quad e_2 = 0.000609. \quad (\text{A17})$$

The transition region to branched polymer behavior appears to be broad. For definiteness, the smallest distance in the fit domain was chosen to be at the right inflexion point of $n(r)$, $r = 25$. The volume of the region $r > 25$ is a substantial fraction of the total volume: $(N_4 - N(25))/N_4 = 0.34$.

Besides fitting $n(r)$ with constant-curvature forms, detailed scale factors $a(r)$ were also studied in [42] through interpolation of $n(r)^{1/3}$. Figure 24 shows $n(r)^{1/3}$ together with the above fits to the left and right flanks of $n(r)$. The fit near the maximum is discussed in appendix B.

In the following $\tilde{n}(r)$ is used instead of $n(r)$ as it avoids having to discuss some discretization effects later in (A22). For convenience an interpolation of $\tilde{n}(r)^{1/3}$ is denoted by $\tilde{n}_{1/3}(r)$. The lattice scale factor for a metric of the form (1) is proposed to be given by

$$a(r - \tilde{s}) = c^{-1/3} \tilde{n}_{1/3}(r), \quad (\text{A18})$$

where c and \tilde{s} are fit parameters. For these we can use the values (A15) of the short distance fit with fit function (A14), or its ‘tilde version’. Also used was a more ‘agnostic’ version that did not involve a fit function, as follows: linear interpolation of $\tilde{n}_{1/3}$ and extrapolation into the region $r < 1/2$ results in a zero at $r = \tilde{s}$, $\tilde{n}_{1/3}(\tilde{s}) = 0$, and

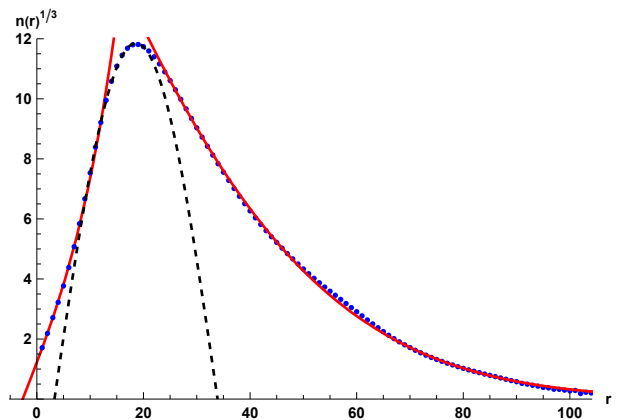


FIG. 24. Central values $n(r)^{1/3}$ of the $n(r)$ data in figure 23 (blue dots); $c^{1/3} r_0 \sinh[(r-s)/r_0]$ from the fit to $n(r)$ by (A14) in the region $2 \leq r \leq 10$ (red curve on the left flank) and $\exp[(1/3)(e_0 - e_1 r - e_2 r^2)]$ from the fit to $n(r)$ by (A16) in the region $25 \leq r \leq 110$. The dashed-black curve represents the cubed-cosine fit (B1)∪(B9) in appendix B, shown for $n(r)$ in figure 27.

c follows from requiring $a(r - \tilde{s})$ to vanish at $r = \tilde{s}$ with unit slope,

$$a(0) = 0, \quad a'(0) = 1. \quad (\text{A19})$$

These requirements ensure that the space with scale factor $a(r)$ extended to \tilde{s} has no conical singularity. Typically \tilde{s} is negative with magnitude a few ℓ , and for the case in figure 23 the parameters come out with the value of s shifted by about $-1/2$ compared to (A15), $\tilde{s} = -3.1$, $c = 0.11$. Subsequently the discrete values of $\tilde{n}_{1/3}(r)$ at half-integer values are interpolated by a polynomial of sufficiently high order.

To enable using continuum formulas, such as $\int d\Omega_3 = 2\pi^2$ when calculating a volume as in (2), a and r were scaled in [42] by a factor λ . The resulting quantities were dubbed ‘continuum’ and indicated by a subscript ‘c’,

$$r_c = \lambda(r - s), \quad a_c(r_c) = \lambda a(r - s), \quad r_{0c} = \lambda r_0, \quad (\text{A20})$$

The factor λ was defined as

$$\lambda^4 = \frac{c v_4}{2\pi^2}, \quad (\text{A21})$$

which gives $\lambda = 0.34$ for the case in figure 23. An r -dependent $\lambda(r)$ can be defined by comparing the continuum volume $V_c(r_c)$ with the lattice $N(r)v_4$:

$$\begin{aligned} V_c(r_c) &= 2\pi^2 \int_0^{r_c} d\bar{r}_c a_c(\bar{r}_c)^3 = 2\pi^2 \frac{\lambda(r)^4}{c} \int_{\tilde{s}}^r d\bar{r} \tilde{n}_{1/3}(\bar{r})^3 \\ &\equiv N(r)v_4 \Rightarrow \frac{\lambda(r)^4}{\lambda^4} = \frac{N(r)}{\int_{\tilde{s}}^r d\bar{r} \tilde{n}_{1/3}(\bar{r})^3}. \end{aligned} \quad (\text{A22})$$

The ratio $\lambda(r)^4/\lambda^4$ is plotted in figure 25; it is close to unity for $r \gtrsim 5$. Employing $n_{1/3}(r)$ in stead of $\tilde{n}_{1/3}(r)$

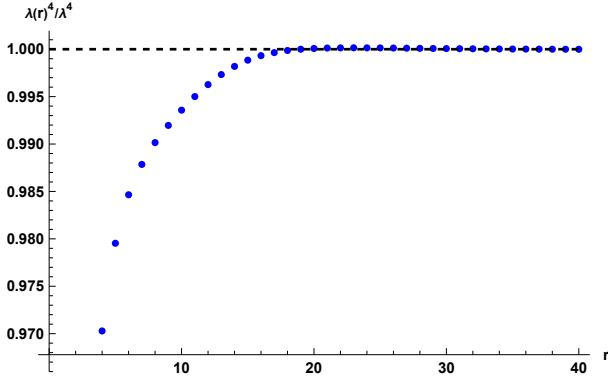


FIG. 25. The ratio $\lambda(r)^4/\lambda^4$ in (A22); $N_4 = 32\text{ k}$, $\kappa_2 = 1.240$.

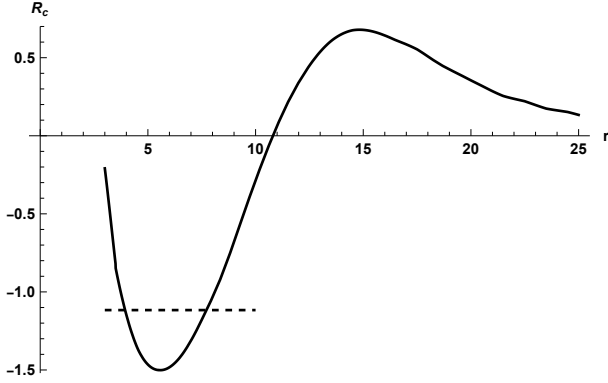


FIG. 26. Curvature R_c versus r from $a_c = \lambda c^{-1/3} \tilde{n}_{1/3}$ with c and λ from the ‘agnostic’ values below (A19), and $-12/r_{0c}^2$ from the short-distance fit (A15). $N_4 = 32\text{ k}$, $\kappa_2 = 1.240$.

would produce a $\lambda(r)$ that approaches λ at much larger distances.

The resulting scale factor $a_c(r_c)$ can be used to compute the curvature using (19), in which we should interpret $a(r)$ as $a_c(r_c)$. Judging results in plots it is convenient to depict $R_c = R/\lambda^2$ as a function of the original r ; $R_c = R(r - \tilde{s})/\lambda^2$ is plotted in figure 26 (large wiggly black curve). It shows negative curvature around $r = 6$ and a change to positive curvature already at $r = 11$. The horizontal black dashed line in the region $r \leq 10$ is $-12/r_{0c}^2$ with curvature radius from the short-distance fit with the hyperbolic-sine function, cf. (A14), (A15).

Appendix B: EdS fit and scaling

In this appendix, inspired by the results in [7], we concentrate on the medium-distance region.

We interpolate $n(r)^{1/3}$ and denote the result by $n_{1/3}(r)$. The positions of the maximum r_m and inflexion points r_{ms}^\pm , defined by $n'_{1/3}(r_m) = 0$ and $n''_{1/3}(r_{ms}^\pm) = 0$, are helpful anchors for analysis. The medium distance region is defined as $r_{ms}^- < r < r_m$. Alternatively $\tilde{n}(r - 1/2) = n(r)$ will be used and its results called the

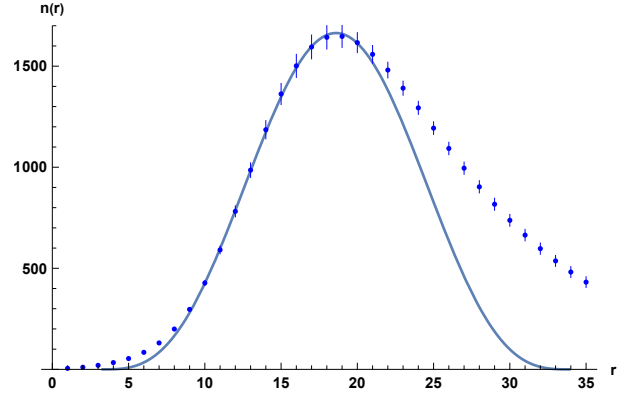


FIG. 27. Plot of $n(r)$ ($\kappa_2 = 1.24$, $N_4 = 32\text{ k}$, $r_m = 18.6$), fitted in the domain $r \in \{10, 11, \dots, 20\}$ by $c[r_0 \cos((r - r_m)/r_0)]^3$, $c = 1.80$, $r_0 = 9.74$ ($s = 3.30$, $\lambda = 0.679$).

tilde version in the following.⁸

In the medium-distance region we have fitted $n(r)$ by the S^4 fit function

$$c f(r - s; r_0) = c r_0^3 \sin[(r - s)/r_0]^3, \quad (\text{B1})$$

which is derived from the EdS scale factor in the continuum, $a_c(r_c) = r_{0c} \sin(r_c/r_{0c})$.

Let us first summarise the construction of the continuum candidate of a metric scale factor $a_c(r_c)$ based on the volume-distance correlator [42]:

$$n(r) \simeq c f(r - s; r_0), \quad r \in [\text{fit-domain}], \quad (\text{B2})$$

$$a(r - s) = c^{-1/3} n_{1/3}(r), \quad (\text{B3})$$

$$a_c(r_c) = \lambda a(r - s), \quad r_c = \lambda(r - s), \quad r_{0c} = \lambda r_0, \quad (\text{B4})$$

$$V_c(r_c) = 2\pi^2 \int_0^{r_c} d\bar{r}_c a_c(\bar{r}_c)^3, \quad V(r) = N(r) v_4 \quad (\text{B5})$$

$$\Delta V_c(r_c) = \Delta V(r), \quad V'_c(r_c) = \frac{1}{\lambda} V'(r), \quad (\text{B6})$$

$$V'_c(r_c) = 2\pi^2 a_c(r_c)^3 = \frac{v_4}{\lambda} N'(r) = \frac{v_4}{\lambda} n(r), \quad (\text{B7})$$

$$\lambda^4 = \frac{c v_4}{2\pi^2}. \quad (\text{B8})$$

In the first line (B2) f is a fit function, chosen to fit $n(r)$ in some domain $r \in \{r_{\min}, \dots, r_{\max}\}$ with fit parameters c and r_0 , and possibly others such as s (f is assumed to vanish at $r = s$). The lattice version of the scale factor is defined in (B3), in which $n(r)$ is supposed to be interpolated. Writing $a(r - s)$ instead of $a(r)$ is a convention. In the third line (B4), lengths in the lattice expressions are scaled by a factor λ to get a scale-factor that satisfies the volume ‘condition’ (B6) which incorporates the integral over angles, $\int d\Omega_3 = 2\pi^2$; Δ indicates the change in the

⁸ Statistical errors on our $n(r)$ data tend to make r_{ms}^\pm somewhat shaky but r_m and r_{ms}^- are sufficiently well determined for our purpose.

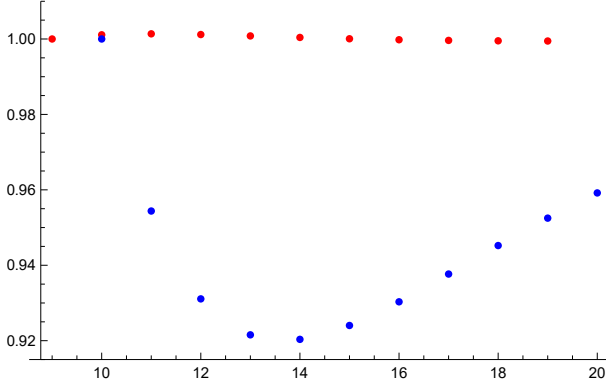


FIG. 28. The ratio (B11) (lower dots, blue) and its ‘tilde-version’ (upper, red) in their respective fit domains. $\{N_4, \kappa_2\} = \{32k, 1.24\}$.

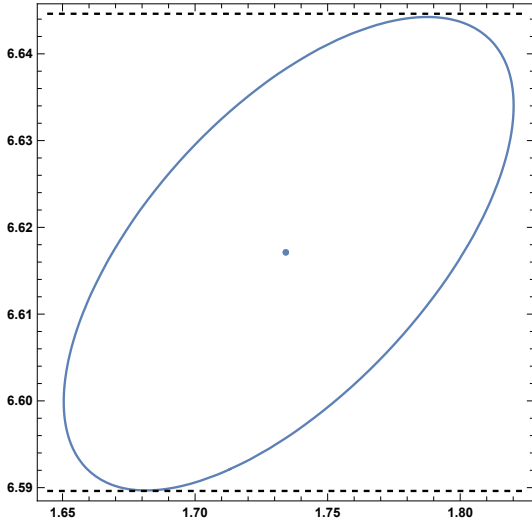


FIG. 29. Contour plot of $\Delta\chi^2 \equiv \chi^2 - \chi_{\min}^2 = 2.30$ in the $(c, \lambda(c)r_0)$ plane; $\lambda(c) \equiv (v_4 c / (2\pi^2))^{1/4}$. Dashed lines indicate error bounds ± 0.028 on r_{0c} . The central point is at $\Delta\chi^2 = 0$: $c = 1.73$, $r_0 = 9.84$, $r_{0c} = \lambda r_0 = 6.62$. The minimal $\chi_{\min}^2 = 2.15$. ‘Tilde version’. $\{N_4, \kappa_2\} = \{32k, 1.24\}$.

fit domain, e.g. $\Delta V(r) = [N(r) - N(r_{\min})] v_4$. The second equality in (B6) used $d/dr_c = (1/\lambda) d/dr$. The relation $N'(r) = n(r)$ in (B7) is a choice (in the tilde version it is a consequence of a linear interpolation of $N(r)$). Substitution of (B3) and (B4) in (B7) leads to the identification of λ in (B8). It assumes that the implicit integral over the interpolated $n(r)$, or its tilde version, is close to $N(r) v_4$ for the volume ‘condition’ (B6) to be satisfied accurately. In any case $a_c(r_c)$ is defined by λ in (B8) together with (B2) – (B4). It can be used to calculate other observables such as the curvature R_c using (19) with $a(r) \rightarrow a_c(r_c)$.

Having determined r_m from the maximum in the interpolated $n(r)$ it is possible to avoid fits with three parameters, $\{r_0, c, s\}$ in (B1), replacing them by fits with

only two, $\{r_0, c\}$:

$$\sin\left(\frac{r-s}{r_0}\right) = \cos\left(\frac{r-r_m}{r_0}\right) \ \& \ s = r_m - r_0\pi/2. \quad (\text{B9})$$

For the example $N_4 = 32k$, $\kappa_2 = 1.24$, the discrete fit domain is taken to be bounded by $r_{\text{ms}}^- (= 9.97)$ and $r_m + 1 (= 19.6)$ rounded off to integers r_{\min} and r_{\max} : $r \in \{10, 11, \dots, 20\}$. For the tilde version the boundary of the fit domain comes out as $\{r_{\min}, r_{\max}\} = \{9, 19\}$. The fit using the equivalent cosine form in (B9) is shown in figure 27 and its comparison with $n(r)^{1/3}$ in figure 24. Note that in (B9) $r - r_m = r - 1/2 - \tilde{r}_m$ (the difference due to interpolation effects in $n_{1/3}(r)$ and $\tilde{n}_{1/3}(r)$ is negligible). The fitted parameters come out as (*tilde version*)

$$c = 1.73, \ r_0 = 9.84 \Rightarrow s = 2.65, \ \lambda = 0.673; \quad (\text{B10})$$

c and s here differ qualitatively from the ones in (A15).

A check on the volume ‘condition’ (B6) is given by the ratio

$$\frac{N(r_{\min})v_4 + 2\pi^2\lambda \int_{r_{\min}}^r d\bar{r} a_c(\bar{r} - s)^3}{N(r)v_4} \quad (\text{B11})$$

(the integral is $\Delta V_c(r_c)$), which, similar to (A22) should be close to 1 in the fit domain $\{r_{\min}, r_{\min} + 1, \dots, r_{\max}\}$. This ratio is shown in figure 28 and we see again that the ‘tilde version’ of the above procedure gives more accurate results.

The parameters c and r_0 are quite (anti-)correlated. The correlation is reduced between c and $r_{0c} = \lambda r_0$. Figure 29 shows a contour corresponding to 68.3% confidence level if statistics is Gaussian. The relative error of r_{0c} is about half that of r_0 obtained from a similar plot; the absolute error is again smaller by the factor λ ,

$$r_{0c} = 6.618 \pm 0.028. \quad (\text{B12})$$

The constant curvature $+12/r_{0c}^2$ and the local curvature $R_c = R/\lambda^2$ are shown in figure 30 (respectively by the purple-dashed line in $9 \leq r \leq 19$ and the purple curve in $5 < r < 25$). For comparison the figure also shows the curvature following from the propagator metric $c_G a_G(r)$ with the fiducial value of c_G determined in section III.

Putting $r_{0c} = \lambda s_0 N_4^{1/4}$ can re-write the fit function:

$$\begin{aligned} n(r) &= c r_0^3 \sin^3\left(\frac{r-s}{r_0}\right) = \frac{\lambda}{v_4} 2\pi^2 r_{0c}^3 \sin^3\left(\frac{r_c}{r_{0c}}\right) \\ &= \frac{3}{4} \eta_L N_4 \frac{1}{s_0 N_4^{1/4}} \sin^3\left(\frac{i}{s_0 N_4} + b\right), \end{aligned} \quad (\text{B13})$$

$$\begin{aligned} \eta_L &= \frac{V_c(S^4)}{V}, \quad V_c(S^4) = \frac{8\pi^2}{3} r_{0c}^4, \quad V = N_4 v_4, \\ i &= r; \quad b = \frac{-\lambda s}{r_{0c}}, \quad \lambda s_0 N_4^{1/4} = r_{0c}, \end{aligned} \quad (\text{B14})$$

where $V_c(S^4)$ is the volume of a four-sphere with radius r_{0c} . The notation in (B13) is that of equation (19) in

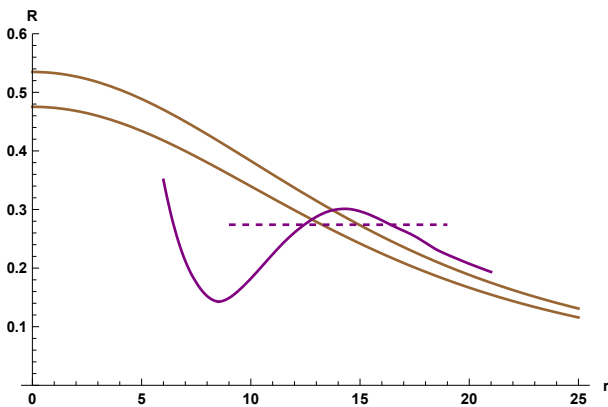


FIG. 30. Curvatures versus r from $a_c(r_c)$ in (B4) and $12/r_{0c}^2$, with c and λ from the EdS fit values (B10) for $\{N_4, \kappa_2\} = \{32k, 1.24\}$. Wiggly purple curve: $R_c(r_c) = R(r)/\lambda^2$. Horizontal purple dashed line in $9 \leq r \leq 19$: $+12/r_{0c}^2$ with $r_{0c} = 6.62$ in (B12). Also shown is curvature from the new scale factor $a(r) = c_G a_G(r)$ for fiducial examples of c_G . The slowly varying brown curves starting near 0.5 represent $R(r)$ with $c_G = 1.46$ (upper) and 1.55 (lower).

[7] where this fit function was used at the boundary of the phase transition. (The identification cannot be perfect since i is an integer in [7], which used degenerate triangulations, whereas here r is integer and λ is real.)

Repeating the above procedure for other values of $\{N_4, \kappa_2\}$, in our limited collapsed phase data base, we find similar results: cubed-cosine fits appear to be accurate in the medium distance region with well determined curvature radii r_{0c} .⁹ For a sample in which the choice of κ_2 was guided by seeking similar values of the fit-boundary ratios $r_{ms}^-/r_m \equiv x_{ms}$, tilde-version results came out as

$\langle N_4 \rangle$	κ_2	x_{ms}	r_m	s	λ	r_{0c}
7906	1.17	0.472	13.9	0.8	0.571	4.746 ± 0.022
15909	1.20	0.523	15.5	2.2	0.666	5.645 ± 0.013
31918	1.24	0.522	18.1	2.7	0.673	6.618 ± 0.028
63911	1.266	0.525	20.5	3.5	0.718	7.795 ± 0.017

(B15)

Here $\langle N_4 \rangle = 1 + \sum_r n(r)$ is the actual simulation average.

Figure 31 shows r_{0c} versus $\langle N_4 \rangle$ (blue dots with error bars). The blue curve (practically overlaid by the dashed black curve) represents a fit by the function

$$r_{0c} = c_s^{r_{0c}} \langle N_4 \rangle^{1/d_s}, \quad (\text{B16})$$

which gives $d_s = 4.266 \pm 0.052$ with a χ^2 of 3.9 (the error comes from a $(c_s^{r_{0c}}, d_s)$ contour plot as in figure 29). A good-looking fit ($\chi^2 = 5.8$) is also obtained by the

⁹ A skeptic might question the interpretation of r_0 – hence also r_{0c} – by claiming that a quadratic approximation $\cos(x) \rightarrow 1 - x^2/2$, $x = (r - r_m)/r_0$, gives equally good medium-distance fits: this is not so, the cosine fits have smaller χ^2 .

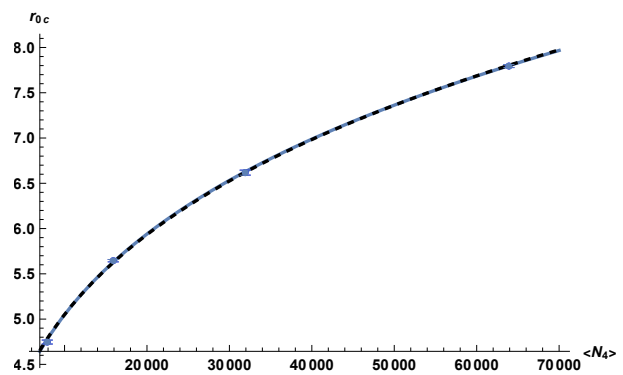


FIG. 31. Scaling test of curvature radii r_{0c} in the medium distance region. Data from table B15 fitted by $r_{0c} = c_s^{r_{0c}} \langle N_4 \rangle^{1/d_s}$ (blue), and by $r_{0c} = c_{-1}^{r_{0c}} \langle N_4 \rangle^{1/4} + c_0^{r_{0c}}$ (black-dashed); $c_s^{r_{0c}} = 0.583$, $d_s = 4.266 \pm 0.052$, $c_{-1}^{r_{0c}} = 0.466$, $c_0^{r_{0c}} = 0.388$.

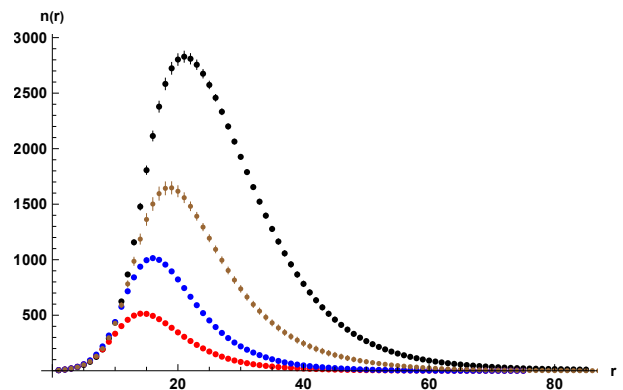


FIG. 32. The four $n(r)$ of table (B15); bottom to top at $r \approx 20$: $\kappa_2 = 1.17$ (red), 1.20 (blue), 1.240 (brown) and 1.266 (black).

first two terms of a finite-volume expansion in powers of $\langle N_4 \rangle^{-1/4}$,

$$r_{0c} = c_{-1}^{r_{0c}} \langle N_4 \rangle^{1/4} + c_0^{r_{0c}} + \dots, \quad (\text{B17})$$

as shown by the black dashed curve. The finite-volume correction $c_0^{r_{0c}}$ is needed here. Omitting it and trying one-parameter fits on three, or even only two, values of N_4 gives immediately unacceptable looking fits with at least doubled χ^2 values.

The results can be used to study scaling. The $n(r)$ of table (B15) are shown in figure 32. In [42] we used r_m for a scaling length r_* in

$$\rho(z) = \frac{r_*}{N_4} n(z r_*), \quad (\text{B18})$$

with somewhat different $\kappa_2 = 1.21, 1.30$ and 1.260, respectively at $N_4 = 16k, 32k$ and 64k, that were chosen to match the entire scaled $n(r)$ curves. This $r_* = r_m$ can be viewed as ‘agnostic’ since it does not involve approximating $n(r)$ by some fit function.

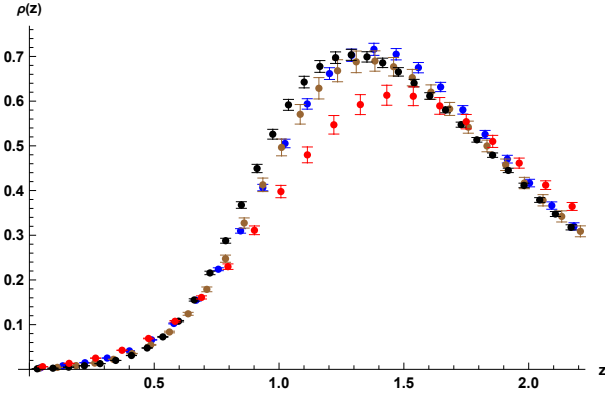


FIG. 33. $\rho(z)$ with $r_* = N_4^{1/4}$ in (B18) and $N_4 \rightarrow \langle N_4 \rangle$. Bottom to top near $z = 1$: $\kappa_2 = 1.17, 1.240, 1.20, 1.266$. Colors as in figure 32.

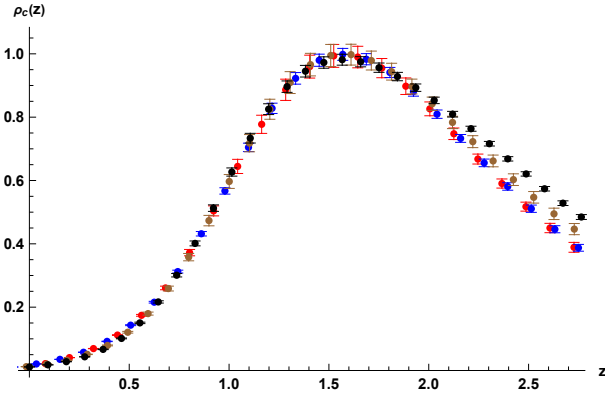


FIG. 34. $\rho_c(z)$ in (B20). Top to bottom in $z \in (1, 1.1)$: $\kappa_2 = 1.17, 1.266, 1.240, 1.20$. Colors as in figure 32.

In [7], good scaling including all distances is obtained when using $r_* = N_4^{1/4}$ at the $\beta = 0$ phase boundary, where the scaling dimension (‘fractal’ or ‘global’ Hausdorff dimension) is compatible with four. Here, using $N_4^{1/4}$ does not lead to good scaling, cf. figure 33, which is no surprise given the need for a second term in the finite-volume expansion (B17).

However, $n(r)$ is not a ‘continuum’ observable such as $V'_c(r_c)$, i.e. $2\pi^2 a_c(r_c)^3$. Using r_{0c} as a scaling length, and (B3) – (B8), in particular (B4) for converting to the lattice r ,

$$r_c = z r_{0c}, \quad r = z r_0 + s, \quad (\text{B19})$$

we arrive at the scaled observables:

$$\rho_c(z) = \frac{a_c(z r_{0c})^3}{r_{0c}^3} = \frac{n(z r_0 + s)}{c r_0^3}, \quad (\text{B20})$$

$$\rho_a(z) = \frac{a_c(z r_{0c})}{r_{0c}} = \frac{n(z r_0 + s)^{1/3}}{c^{1/3} r_0}, \quad (\text{B21})$$

$$\begin{aligned} \rho_R(z) &= r_{0c}^2 R_c(z r_{0c}) \\ &= 6 \left[-\frac{\rho_a''(z)}{\rho_a(z)} - \frac{\rho_a'(z)^2}{\rho_a(z)^2} + \frac{1}{\rho_a(z)^2} \right]. \end{aligned} \quad (\text{B22})$$

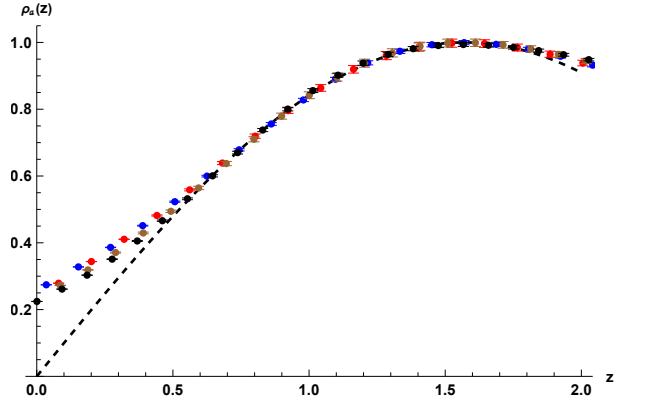


FIG. 35. Scaled metric scale-factor $\rho_a(z)$ in (B21). Top to bottom near $z = 0.2$: $\kappa_2 = 1.17, 1.20, 1.240, 1.266$. Colors as in figure 32. The black-dashed curve represents the scaled fit-functions, $\sin(z)$.

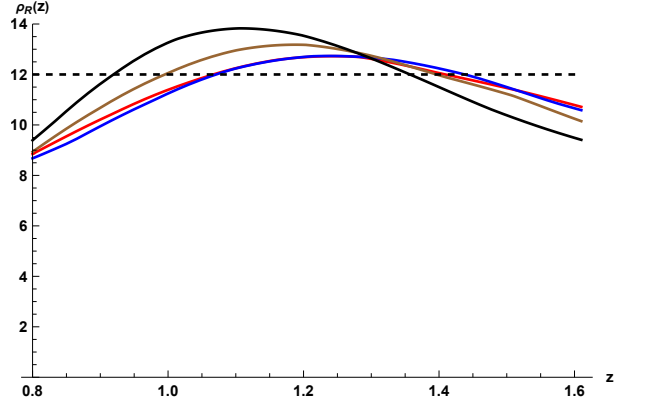


FIG. 36. Scaled scalar curvature $\rho_R(z)$ in (B22) in the intersection of the scaled fit domains. Bottom to top at $z = 0.9$: $\kappa_2 = 1.20, 1.17, 1.240, 1.266$. Colors as in figure 32. The constant curvature of the scaled fit functions corresponds to the dashed line.

Note that in this scaling the argument of the volume-distance correlator involves the shift s : $n(z r_0 + s)$.

Figure 34 shows nice scaling for $V'_c/(2\pi^2) = a_c^3$ at medium distances. Figure 35 compares the scaled a_c with scaled fit functions, which are all equal to $\sin(z)$. The scaled data appear to approach $\sin(z)$ as the volume increases.

There is no reason why the limiting $\rho_a(z)$ should become *exactly* $\sin(z)$ in $0 < z < \pi/2$. One would expect it does not when there is a nontrivial condensate that differs from a mere cosmological constant.

As shown in figure 36, the scaled local curvatures $r_{0c}^2 R_c(r_c)$ of the two smallest volumes match closely in the intersection of the fit domains $0.80 < z < 1.61$, but those of two larger volumes differ substantially. For the case $\{N_4 = 32k, \kappa_2 = 1.24\}$ the curvature R_c is also shown in figure 30 as a function of r (in this case the intersection region corresponds to $11 < r < 19$).

Appendix C: Massless propagators [44]

On a space with constant negative curvature, a massless propagator shows exponential fall off with the distance and can thus be viewed as having a mass.

Rewriting the equation for the massless propagator $\square G(x^\mu) = 0$ using spherical symmetry and a space of constant negative curvature with curvature radius r_0 we get

$$\left[\frac{d}{dr} + \frac{3 \coth(r/r_0)}{r_0} \right] \frac{d}{dr} G(r) = 0. \quad (\text{C1})$$

This can be exactly solved and using the boundary conditions

$$G(r) \rightarrow 0, \quad r \rightarrow \infty, \quad (\text{C2})$$

$$G(r) \rightarrow \frac{1}{4\pi r^2}, \quad r \rightarrow 0, \quad (\text{C3})$$

and the solution is

$$G(r) = \frac{1}{4\pi r_0^2} \left\{ 2 \frac{\exp(r/r_0) + \exp(-r/r_0)}{(\exp(r/r_0) - \exp(-r/r_0))^2} \right. \quad (\text{C4})$$

$$\left. - \ln \frac{1 + \exp(-r/r_0)}{1 - \exp(-r/r_0)} \right\}. \quad (\text{C5})$$

Expanding this around $r \rightarrow \infty$ in $\exp(-r/r_0)$ results in

$$G(r) = \frac{2}{4\pi r_0^2} \sum_{n=0}^{\infty} \frac{n(n+1)}{2n+1} \exp(-(2n+1)r/r_0). \quad (\text{C6})$$

We see that for large r the massless propagator behaves as

$$G(r) \propto \exp(-3r/r_0), \quad r \rightarrow \infty. \quad (\text{C7})$$

If we define the mass m from the long distance behaviour of the propagator using $G(r) \propto \exp(-mr)$, then this mass and the curvature radius are related by $mr_0 = 3$.

On the lattice, we solved the Laplace equation $\square G(x^\mu) = 0$ using the algebraic multigrid routine AMG1R5. Figure 37 shows the results for the smallest volume $N_4 = 32000$. Note that we can add an arbitrary constant to $G(r)$. This constant is determined by the details of the computer code and has no physical meaning. This also means that the individual values of the data points have no meaning and therefore we have left out the error bars. This is not an obstacle to calculating the masses and their errors.

We fitted this data to $a \exp(-mr) + c$ in the range $6 \leq r \leq 20$. The fits are also shown in figure 37.

Figure 38 show the masses m measured for various values of κ_2 at the two volumes that were used. The error bars were obtained by the jackknife method, leaving out one configuration each time. In this way the correlation between the data of two different origins on the same configuration does not artificially decrease the errors.

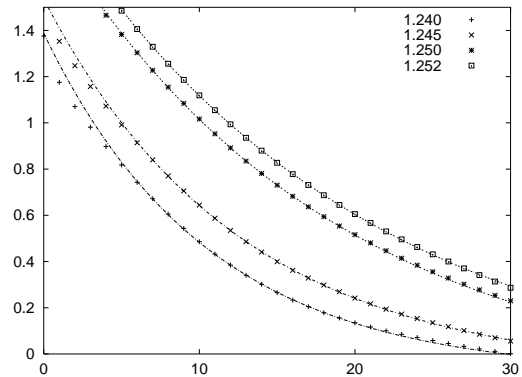


FIG. 37. Averaged massless lattice propagators $G(r)$ for some values of κ_2 at $N_4 = 32000$.

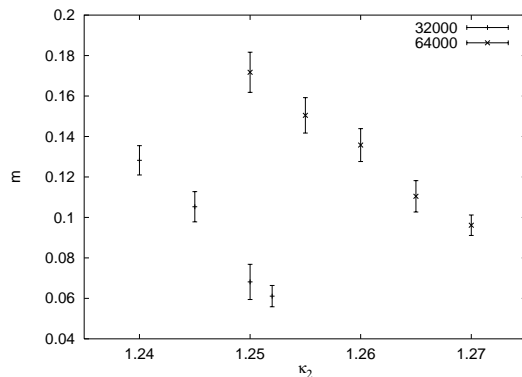


FIG. 38. Measured effective masses of propagators as a function of κ_2 for two values of N_4 .

The configurations used for these measurements were recorded each 5000 sweeps, where a sweep consists of N_4 accepted moves. For each configuration we used 200 different origins to calculate the propagator from. We could only measure these masses for a limited number of κ_2 values, because the calculation of the propagator takes much CPU time.

Appendix D: Comparison of effective masses with curvature radii

The original motivation of the propagator study was the negative curvature found in the volume-distance correlation at short distances. In this appendix the exponential behavior of the propagator data is analyzed further.

For a comparison with the asymptotic form (C7) that predicts $mr_0/3 = 1$, we use r_0 results recorded in table (B.2) of [42] for the volume $N_4 = 64k$. Figure 39 shows

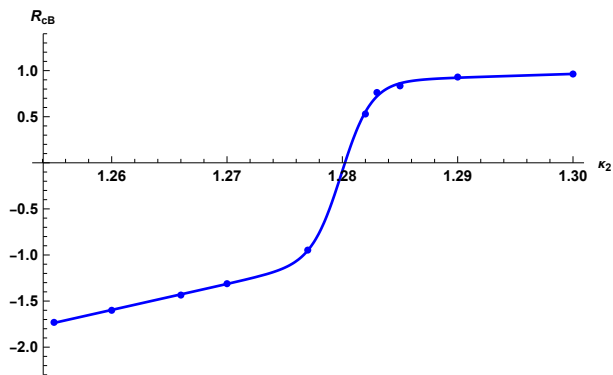


FIG. 39. Curvature R_c vs. κ_2 obtained with the B-fit (dots) fitted by the function (8.6) in [42]: $N_4 = 64k$, data from the Erratum.

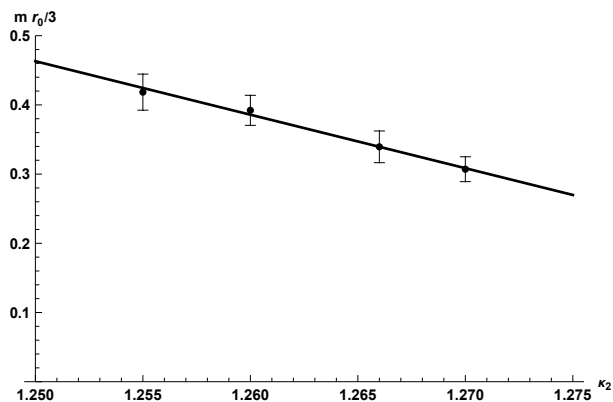


FIG. 40. The ratio $m/(3/r_0)$ vs. κ_2 in the collapsed phase with r_0 values from the fit in figure 39; $N_4 = 64k$. The line is a linear fit by $10 - 7.7 \kappa_2$.

a (so-called ‘continuum curvature’) R_c in both phases.¹⁰

Numerical data files of the propagators and fitted parameters of $a \exp(-mr) + c$ are lost, unfortunately. However, we have retrieved values of m , and for $N_4 = 32k$ also of the propagators, from the postscript files of figure 37 and 38.

Figure 40 shows the ratio $m/(3/r_0)$ vs. κ_2 with the r_0 corresponding to figure 39 in which $N_4 = 64k$. (With $N_4 = 32k$ only $\kappa_2 = 1.240$ and 1.245 volume-distance results are available.) The linearly varying ratio seems to point again to negative curvature. The magnitude of the ratio is much smaller than 1. An immediate explanation is suggested by the fact that the effective-mass fits to the propagators involve larger distances (up to $r = 20$) than the negative-curvature fits to the volume-distance correlator which ended at $r = 12$. We shall conclude below that the discrepancy is even more fundamental.

¹⁰ From figure 14 in [42] we see that for $N_4 = 64k$ all the κ_2 values in figure 38 lay outside the curvature-susceptibility peak on the collapsed side; for $N_4 = 32k$ this holds only for $\kappa_2 = 1.240$ and 1.245 , whereas 1.250 and 1.252 are within the peak.

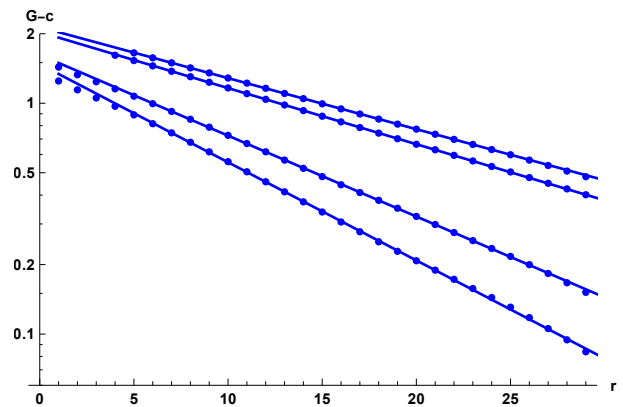


FIG. 41. Propagators fitted by $c + a \exp(-mr)$ in the domain $6 \leq r \leq 24$. Data and fit-function are both subtracted by c ; top to bottom $\kappa_2 = 1.252, 1.250, 1.245, 1.240$; $N_4 = 32k$.

Refitting the retrieved propagator data with the fit function $a \exp(-mr) + c$ in the domain $6 \leq r \leq 24$, the fitted parameters came out as ($N_4 = 32k$):

κ_2	c	a	m	$r_{0m} \equiv 3/m$
1.240	-0.0726	1.48	0.098	30.7
1.245	-0.0816	1.62	0.081	37.2
1.250	-0.148	2.04	0.056	53.5
1.252	-0.167	2.14	0.051	58.9

The effective curvature radii r_{0m} are remarkably large. Our refitted m are 20-30 % smaller than those in figure 38 (the original fit domain $6 \leq r \leq 20$ in section C leads to even slightly smaller values and spoils the good looking fits in figure 41 for $r > 20$). The re-fits are of the least-squares type whereas the error bars in figure 38 represent jack-knife errors, which tend to underestimate errors. Overlaying a print of the plot in figure 37 by a same size print for the propagators obtained with refitted parameters gives a perfect match visually. We ascribe the difference to small mis-representations by the postscript files together with correlations between the fit parameters a , m and c . It does not affect the exploring nature of this work.¹¹

Figure 41 shows the obtained propagators shifted by $-c$ on a logarithmic scale. Exponential behavior is a fairly good approximation as can be seen quantitatively in figure 42 which shows the ratio $(\text{data}-c)/(a \exp(-mr))$ for $\kappa_2 = 1.240$. In this case the deviations from 1 are at the percent level in the fit domain; for the other κ_2 such deviations are smaller by an order of magnitude. The local minimum near $r = 18$ occurs where the volume-distance correlator has its maximum (cf. figure 23 in appendix A).

¹¹ Another example is the fit value of e_1 in figure 3, which corresponds to an $m = 3e_1 = 0.11$ differing 8% from the 0.98 in (D1).

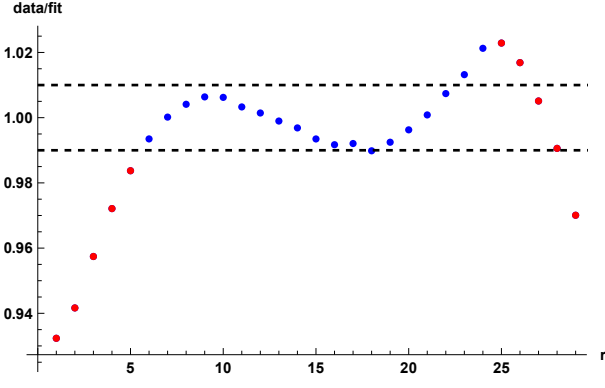


FIG. 42. Subtracted propagator $G(r) - c$ divided by subtracted fit-function $a \exp(-mr)$, for $\kappa_2 = 1.240$. The blue(red) points are inside(outside) the fit domain.

Remarkably, this maximum hardly affects the nearly exponential behavior of the shifted propagators. Surprising is also the fact that this behavior occurs all the way down to about $r = 6$. It implies that using the exact form (C5) of $G(r)$ in a fit function of the form $c + a G(r)$ *cannot fit the data*. This becomes also immediately clear when trying such fits. Last, but not least, one notes that $G(r)$ in (C5) approaches the leading term in its asymptotic expansion to 1% accuracy only for $r/r_0 > 2.59$; for $\kappa_2 = 1.240$ this means $r > 80$!

The goodness of the exponential fit does *not* indicate hyperbolic nature of the geometry.

Appendix E: Einstein tensor for a time-dependent diagonal metric

In equation (14.48) of [57], a time-dependent rotation-invariant diagonal Lorentzian metric depending on coordinates T, R, θ and ϕ is defined by its line element

$$ds^2 = -e^{2\Phi} dT^2 + e^{2\Lambda} dR^2 + r^2(d\theta^2 + \sin(\theta)^2 d\phi^2), \quad (\text{E1})$$

and its Einstein tensor is given in (14.48), (14.51) and (14.52) of this book. Transforming coordinates $T = -it$ and choosing $R = r$ we obtain the Einstein tensor for the Euclidean metric. The transformed functions of [57] are given by

$$\Phi = \frac{1}{2} \ln g_{tt}, \quad \Lambda = \frac{1}{2} \ln g_{rr}, \quad (\text{E2})$$

and

$$E_1 = e^{-2\Phi} (\ddot{\Lambda} + \dot{\Lambda}^2 - \dot{\Lambda}\dot{\Phi}), \quad (\text{E3})$$

$$E_2 = -e^{-2\Lambda} (\Phi'' + \Phi'^2 - \Phi'\Lambda'), \quad (\text{E4})$$

$$E = E_1 + E_2, \quad \bar{E} = -\frac{1}{r} e^{-2\Lambda} \Phi', \quad (\text{E5})$$

$$F_{\text{MTW}} = \frac{1}{r^2} (1 - e^{-2\Lambda}), \quad \bar{F}_{\text{MTW}} = \frac{1}{r} e^{-2\Lambda} \Lambda', \quad (\text{E6})$$

$$H = -i \frac{1}{r} e^{-\Phi-\Lambda} \dot{\Lambda}, \quad (\text{E7})$$

in terms of which Euclidean mixed (up-down) components of the Einstein tensor are given by

$$\begin{aligned} G^t_t &= -F_{\text{MTW}} - 2\bar{F}_{\text{MTW}}, & G^r_r &= -2\bar{E} - F_{\text{MTW}}, \\ G^\theta_\theta &= G^\phi_\phi = -E - \bar{E} - \bar{F}_{\text{MTW}}, & G^t_r &= 2iH. \end{aligned} \quad (\text{E8})$$

Note that E_1 contains two time derivatives of g_{rr} , E_2 two spatial derivatives of g_{tt} , and that their sum $E_1 + E_2$ enters in G^θ_θ . It is convenient to treat $F(a)$ introduced in (33) as a function of $a^2 = r^2 + y^2$, writing

$$F(\sqrt{r^2 + y^2}) = \tilde{F}(r^2 + y^2). \quad (\text{E9})$$

The functions E, \dots, H depend on derivatives of the metric components

$$g \equiv g_{tt}, \quad j \equiv \frac{1}{g_{rr}} \quad (\text{E10})$$

(cf. (34), (36)). Indicating their explicit dependence on variables these are given by

$$j(r, y) = \frac{r^2 \tilde{F}(r^2 + y^2) + y^2}{r^2 + y^2}, \quad (\text{E11})$$

$$g(r, y, \dot{y}) = \frac{\dot{y}^2}{\tilde{F}(r^2 + y^2)} j(r, y). \quad (\text{E12})$$

Since y is a solution of $\partial_r y = P$,

$$P(r, y) = ry \frac{-1 + \tilde{F}(r^2 + y^2)}{y^2 + r^2 \tilde{F}(r^2 + y^2)}, \quad (\text{E13})$$

we can replace spatial derivatives $\partial_r y$ by P :

$$\frac{d}{dr} j = \frac{\partial j}{\partial r} + \frac{\partial j}{\partial y} P, \quad (\text{E14})$$

$$\frac{d}{dr} g = \frac{\partial g}{\partial r} + \frac{\partial g}{\partial y} P + \frac{\partial g}{\partial \dot{y}} \partial_r \dot{y}, \quad (\text{E15})$$

$$\partial_r \dot{y} = \partial_r \partial_t y = \partial_t \partial_r y = \frac{d}{dt} P = \frac{\partial P}{\partial y} \dot{y}, \quad (\text{E16})$$

and recursively for higher derivatives. In principle this gives E_1, E_2, \dots, H as functions depending explicitly only on r, y, \dot{y}, \ddot{y} (\ddot{y} is not needed since double time derivatives occur only on Λ which does not contain \dot{y}). However the explicit dependence on \dot{y} and \ddot{y} cancels out. This should happen in the diagonal components of the Einstein tensor which transform as a scalar field under time transformations $\tilde{t}(t)$ and \tilde{y} and \tilde{y} are not such scalars. But it happens already in the individual E_1, E_2, \dots, H .

Further details of E_1, \dots, H are in appendix F. There is a near cancellation between E_1 and E_2 , hence also in their sum $E = E_1 + E_2$ contributing to G^θ_θ . This is relevant because E_1 and E_2 separately are increasingly strongly peaked as $t \rightarrow 0$, whereas E clearly reaches a finite limiting form. The Dirac distribution $\delta(r - h)$ conjectured in (85) as a result of the double spatial derivative in E_2 , is not present in E , hence also not in G^θ_θ at $t = 0$.

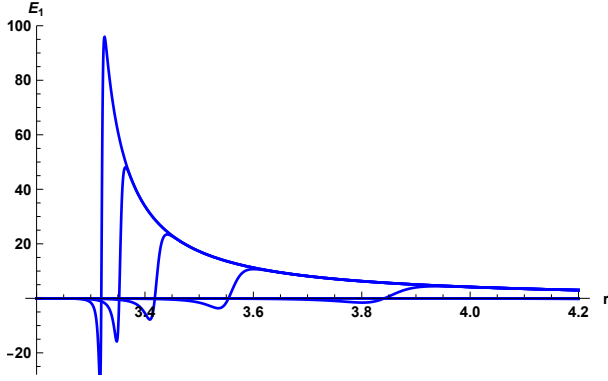


FIG. 43. Plot of $E_1(r, t)$ for $r_p = 2h$ and $t = 10^{k-24}$, $k = 0, 4, 8, 12, 16$.

We were not able to prove that $\delta(r - h)$ emerges in E_1 and E_2 separately as $t \rightarrow 0$, although there is modest numerical evidence for a finite limit in the distributional sense.

The components of G^μ_ν listed in (E8) become:

$$G^t_t = \frac{(\tilde{F} - 1)(3y^2 + r^2\tilde{F})}{(y^2 + r^2)(y^2 + r^2\tilde{F})} + \frac{2r^2\tilde{F}\tilde{F}'}{y^2 + r^2\tilde{F}}, \quad (\text{E17})$$

$$G^r_r = \frac{(\tilde{F} - 1)(y^2 + 3r^2\tilde{F})}{(y^2 + r^2)(y^2 + r^2\tilde{F})} + \frac{2y^2\tilde{F}'}{y^2 + r^2\tilde{F}}, \quad (\text{E18})$$

$$G^\theta_\theta = G^\phi_\phi = \frac{\tilde{F} - 1}{y^2 + r^2} + 2\tilde{F}', \quad (\text{E19})$$

$$G^t_r = 2ry\sqrt{\tilde{F}} \left[\frac{\tilde{F} - 1}{(y^2 + r^2)(y^2 + r^2\tilde{F})} - \frac{\tilde{F}'}{y^2 + r^2\tilde{F}} \right]. \quad (\text{E20})$$

Here \tilde{F}' is the derivative of \tilde{F} with respect to its argument: $\tilde{F}'(r^2 + y^2) = d\tilde{F}(x)/dx|_{x \rightarrow r^2 + y^2}$ (and similar for \tilde{F}'' which appears in E_1 and E_2). The trace of the Einstein tensor simplifies to

$$G^\mu_\mu = \frac{6(-1 + \tilde{F})}{y^2 + r^2} + 6\tilde{F}'. \quad (\text{E21})$$

Following the reasoning in section IV B, the limit-forms for $t \rightarrow 0$ in that section follow here easily – without encountering singularities – by letting $y \rightarrow 0$ in the exterior region, and $\tilde{F} \rightarrow 0$ & $y \rightarrow \sqrt{h^2 - r^2}$ in the interior region. The off-diagonal component G^t_r vanishes in the limit. The possibility of a remaining finite distribution at $r = h$ is investigated in appendix F.

Appendix F: Details of E_1, \dots, H

After the canceling-out of \dot{y} and \ddot{y} , E_1 and E_2 are given by

$$E_1 = e_{10} + e_{11}\tilde{F}' + e_{12}(\tilde{F}')^2,$$

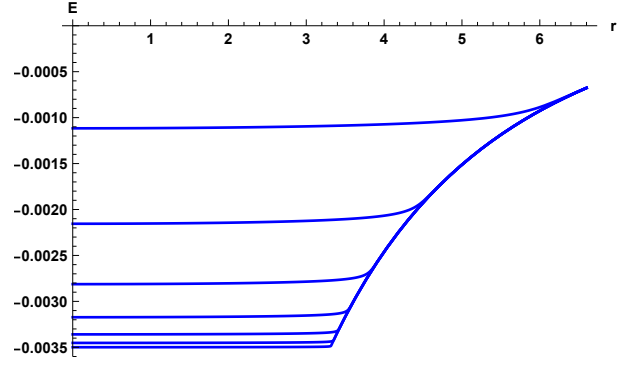


FIG. 44. Plot of $E = E_1 + E_2$ for the same times as in figure 43.

$$\begin{aligned} E_2 &= e_{20} + e_{21}\tilde{F}' + e_{22}(\tilde{F}')^2, \\ e_{10} &= \frac{1}{(y^2 + \tilde{F}r^2)^3} \left[r^2(3y^2(-1 + \tilde{F})\tilde{F} - (-1 + \tilde{F})\tilde{F}^2r^2) \right. \\ &\quad \left. + \tilde{F}''r^2(2y^6\tilde{F} + 2y^4\tilde{F}(1 + \tilde{F})r^2 + 2y^2\tilde{F}^2r^4) \right], \\ e_{11} &= \frac{1}{(y^2 + \tilde{F}r^2)^3} \left[r^2(y^4(1 - 4\tilde{F}) + \tilde{F}^2r^4 \right. \\ &\quad \left. + y^2\tilde{F}(-6r^2 + 4\tilde{F}r^2)) \right], \\ e_{12} &= \frac{1}{(y^2 + \tilde{F}r^2)^3} \left[r^2(y^6 + y^4(1 - 3\tilde{F})r^2 - 3y^2\tilde{F}r^4) \right], \\ e_{21} &= \frac{1}{(y^2 + \tilde{F}r^2)^3} \left[(-y^6 + y^4(-1 + \tilde{F})r^2 \right. \\ &\quad \left. + y^2\tilde{F}r^2(6r^2 - 7\tilde{F}r^2) - \tilde{F}^2r^4(r^2 + \tilde{F}r^2)) \right], \\ e_{20} &= -e_{10}, \quad e_{22} = -e_{12}, \quad e_{11} + e_{21} = -1, \\ E &= E_1 + E_2 = -\tilde{F}'. \end{aligned} \quad (\text{F1})$$

The expressions for \bar{E}, \dots, H come out as:

$$\begin{aligned} \bar{E} &= -\frac{(-1 + \tilde{F})\tilde{F}r^2}{(y^2 + r^2)(y^2 + \tilde{F}r^2)} - \frac{y^2\tilde{F}'}{y^2 + \tilde{F}r^2}, \\ F_{\text{MTW}} &= \frac{1 - \tilde{F}}{y^2 + r^2}, \\ \bar{F}_{\text{MTW}} &= -\frac{y^2(-1 + \tilde{F})}{(y^2 + r^2)(y^2 + \tilde{F}r^2)} - \frac{\tilde{F}\tilde{F}'r^2}{y^2 + \tilde{F}r^2}, \\ iH &= ry\sqrt{\tilde{F}} \left[\frac{\tilde{F} - 1}{(y^2 + r^2)(y^2 + \tilde{F}r^2)} - \frac{\tilde{F}'}{y^2 + \tilde{F}r^2} \right]. \end{aligned} \quad (\text{F2})$$

For the rat-model \tilde{F} and \tilde{F}' can be written in the form (cf. (49))

$$\tilde{F} = c(\sqrt{x} - h)(\sqrt{x} - \bar{h})^3, \quad x = r^2 + y^2, \quad (\text{F3})$$

$$\tilde{F}' = \frac{c(4\sqrt{x} - 3h - \bar{h})(\sqrt{x} - \bar{h})^2}{2\sqrt{x}}. \quad (\text{F4})$$

Figure 43 shows a plot of E_1 corresponding to five (blue) curves of $y(r, t)$ in figure 6 with $r_p = 2h$. A similar

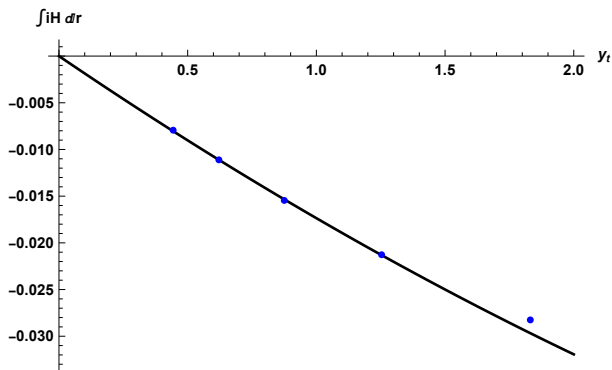


FIG. 45. Plot of $\int_0^{2h} dr iH$ vs. y_t for the same times as in figure 43. The black line represents a fit by $-0.0187 y_t + 0.00139 y_t^2$ to the first four values.

plot for $-E_2(r, t)$ is indistinguishable to the eye, since the sum $E_1 + E_2$ is down in magnitude by a factor of about 10^4 , note the vertical scale in figure 44 which displays E .

The integral $I = \int_{3.2}^{4.2} dr E_1(r, t)$ was monitored to check whether a finite distribution (such as a Dirac function $\delta(r - h)$) develops in E_1 (and also in E_2 as follows from the cancellation) in the limit $t \rightarrow 0$. Considered

as function of $\ln(t)$, I is very well fitted by the form $I = \alpha + \beta \ln(t)$, which suggests a logarithmic divergence in the limit. But a dependence of I as a function of a time t introduced at $r_p = 2h$, ‘far away’ from $r = h$ involves a coordinate peculiarity of this t (cf. figure 7). Testing as a function of the foliation as labeled by the value of y at $r = h$, i.e. $y_t = y(h, t)$, may be a better idea. The values of I are well fitted by the rational-function form $I = (\alpha + \beta y_t)/(1 + \gamma y_t)$, which has a build-in finite limit as $y_t \rightarrow 0$. We take this as a mild support for a finite limit distribution $E_{1,2}$ at $r = h$. However, since only the regular sum E enters in G_θ^θ the finiteness of $E_{1,2}$ is not of physical interest.

The function $2iH = G_r^t$ has been plotted in figure 15. It vanishes when $t \rightarrow 0$ for $r \neq h$ (as also mentioned in appendix E). To investigate the possibility of a finite remaining distribution at $r = h$, consider $I_H = \int_0^{2h} dr iH$. It turns out to be a non-linear function of $\ln(t)$ but an almost linear one as a function of $y_t = y(h, t)$; its four smallest values can be fitted by the form $\beta y_t + \gamma y_t^2$, as shown in figure 45. Adding a constant α to the fit function leads to a rather small value $\alpha = 0.00075$. We assume that H vanishes also as a distribution when $t \rightarrow 0$.

-
- [1] M. E. Agishtein and A. A. Migdal, Simulations of four-dimensional simplicial quantum gravity, *Mod. Phys. Lett.* **A7**, 1039 (1992).
- [2] J. Ambjorn and J. Jurkiewicz, Four-dimensional simplicial quantum gravity, *Phys. Lett.* **B278**, 42 (1992).
- [3] S. Bilke and G. Thorleifsson, Simulating four-dimensional simplicial gravity using degenerate triangulations, *Phys. Rev. D* **59**, 124008 (1999), arXiv:hep-lat/9810049.
- [4] G. Thorleifsson, Lattice gravity and random surfaces, *Nucl. Phys. B Proc. Suppl.* **73**, 133 (1999), arXiv:hep-lat/9809131.
- [5] J. Ambjorn, K. N. Anagnostopoulos, and J. Jurkiewicz, Abelian gauge fields coupled to simplicial quantum gravity, *JHEP* **08**, 016, arXiv:hep-lat/9907027.
- [6] J. Ambjorn, L. Glaser, A. Goerlich, and J. Jurkiewicz, Euclidian 4d quantum gravity with a non-trivial measure term, *JHEP* **10**, 100, arXiv:1307.2270 [hep-lat].
- [7] J. Laiho, S. Bassler, D. Coumbe, D. Du, and J. Neelakanta, Lattice Quantum Gravity and Asymptotic Safety, *Phys. Rev. D* **96**, 064015 (2017), arXiv:1604.02745 [hep-th].
- [8] S. Bilke, Z. Burda, A. Krzywicki, B. Petersson, J. Tabaczek, and G. Thorleifsson, 4d simplicial quantum gravity interacting with gauge matter fields, *Phys. Lett.* **B418**, 266 (1998), arXiv:hep-lat/9710077.
- [9] S. Bilke, Z. Burda, A. Krzywicki, B. Petersson, J. Tabaczek, and G. Thorleifsson, 4d simplicial quantum gravity: Matter fields and the corresponding effective action, *Phys. Lett.* **B432**, 279 (1998), arXiv:hep-lat/9804011.
- [10] D. Coumbe and J. Laiho, Exploring Euclidean Dynamical Triangulations with a Non-trivial Measure Term, *JHEP* **04**, 028, arXiv:1401.3299 [hep-th].
- [11] B. Bruegmann and E. Marinari, 4-d simplicial quantum gravity with a nontrivial measure, *Phys.Rev.Lett.* **70**, 1908 (1993), arXiv:hep-lat/9210002 [hep-lat].
- [12] M. Asaduzzaman and S. Catterall, Euclidean dynamical triangulations revisited, *Phys. Rev. D* **107**, 074505 (2023), arXiv:2207.12642 [hep-lat].
- [13] P. Bialas, Z. Burda, A. Krzywicki, and B. Petersson, Focusing on the fixed point of 4d simplicial gravity, *Nucl. Phys.* **B472**, 293 (1996), arXiv:hep-lat/9601024.
- [14] B. V. de Bakker, Further evidence that the transition of 4D dynamical triangulation is 1st order, *Phys. Lett.* **B389**, 238 (1996), arXiv:hep-lat/9603024.
- [15] T. Rindlisbacher and P. de Forcrand, Euclidean Dynamical Triangulation revisited: is the phase transition really 1st order? (extended version), *JHEP* **1505**, 138, arXiv:1503.03706 [hep-lat].
- [16] J. Ambjorn, A. Goerlich, J. Jurkiewicz, and R. Loll, Non-perturbative Quantum Gravity, *Phys. Rept.* **519**, 127 (2012), arXiv:1203.3591 [hep-th].
- [17] R. Loll, Quantum Gravity from Causal Dynamical Triangulations: A Review, *Class. Quant. Grav.* **37**, 013002 (2020), arXiv:1905.08669 [hep-th].
- [18] J. Ambjorn, Lattice Quantum Gravity: EDT and CDT (2022) arXiv:2209.06555 [hep-lat].
- [19] J. Ambjorn, A. Görlich, J. Jurkiewicz, A. Kreienbuehl, and R. Loll, Renormalization Group Flow in CDT, *Class. Quant. Grav.* **31**, 165003 (2014), arXiv:1405.4585 [hep-th].
- [20] J. Ambjorn, D. Coumbe, J. Gizbert-Studnicki, and J. Jurkiewicz, Searching for a continuum limit in causal dynamical triangulation quantum gravity, *Phys. Rev. D* **93**,

- 104032 (2016), arXiv:1603.02076 [hep-th].
- [21] J. Gizbert-Studnicki, Semiclassical and Continuum Limits of Four-Dimensional CDT (2023) arXiv:2301.06068 [hep-th].
- [22] H. W. Hamber, Scaling Exponents for Lattice Quantum Gravity in Four Dimensions, *Phys. Rev. D* **92**, 064017 (2015), arXiv:1506.07795 [hep-th].
- [23] M. Rocek and R. M. Williams, Quantum Regge Calculus, *Phys. Lett. B* **104**, 31 (1981).
- [24] J. Ambjorn and J. Jurkiewicz, Scaling in four-dimensional quantum gravity, *Nucl. Phys.* **B451**, 643 (1995), arXiv:hep-th/9503006.
- [25] T. Hotta, T. Izubuchi, and J. Nishimura, Singular Vertices in the Strong Coupling Phase of Four-Dimensional Simplicial Gravity, *Nucl. Phys. Proc. Suppl.* **47**, 609 (1996), arXiv:hep-lat/9511023.
- [26] T. Hotta, T. Izubuchi, and J. Nishimura, Singular vertices in the strong coupling phase of four-dimensional simplicial gravity, *Prog.Theor.Phys.* **94**, 263 (1995), arXiv:hep-lat/9709073 [hep-lat].
- [27] S. Catterall, G. Thorleifsson, J. B. Kogut, and R. Renken, Singular Vertices and the Triangulation Space of the D- sphere, *Nucl. Phys.* **B468**, 263 (1996), arXiv:hep-lat/9512012.
- [28] S. Catterall, R. Renken, and J. B. Kogut, Singular structure in 4-D simplicial gravity, *Phys.Lett.* **B416**, 274 (1998), arXiv:hep-lat/9709007 [hep-lat].
- [29] P. Bialas, Z. Burda, B. Petersson, and J. Tabaczek, Appearance of mother universe and singular vertices in random geometries, *Nucl.Phys.* **B495**, 463 (1997), arXiv:hep-lat/9608030 [hep-lat].
- [30] S. Hikami, Conformal Bootstrap Analysis for Single and Branched Polymers, *PTEP* **2018**, 123I01 (2018), arXiv:1708.03072 [hep-th].
- [31] D. Poland, S. Rychkov, and A. Vichi, The Conformal Bootstrap: Theory, Numerical Techniques, and Applications, *Rev. Mod. Phys.* **91**, 015002 (2019), arXiv:1805.04405 [hep-th].
- [32] J. M. Maldacena, The Large N limit of superconformal field theories and supergravity, *Adv. Theor. Math. Phys.* **2**, 231 (1998), arXiv:hep-th/9711200.
- [33] E. Witten, Anti-de Sitter space and holography, *Adv. Theor. Math. Phys.* **2**, 253 (1998), arXiv:hep-th/9802150.
- [34] E. Witten, Anti-de Sitter space, thermal phase transition, and confinement in gauge theories, *Adv. Theor. Math. Phys.* **2**, 505 (1998), arXiv:hep-th/9803131.
- [35] J. Smit, Introduction to quantum fields on a lattice: A robust mate, *Cambridge Lect. Notes Phys.* **15** (2002), [Erratum: <https://www.researchgate.net/profile/Jan-Smit-7>].
- [36] B. V. de Bakker and J. Smit, Gravitational binding in 4D dynamical triangulation, *Nucl. Phys.* **B484**, 476 (1997), arXiv:hep-lat/9604023.
- [37] B. de Bakker and J. Smit, Euclidean gravity attracts, *Nucl. Phys. B Proc. Suppl.* **34**, 739 (1994), arXiv:hep-lat/9311064.
- [38] J. Smit, Three models of non-perturbative quantum-gravitational binding, (2021), arXiv:2101.01028 [gr-qc].
- [39] M. Dai, J. Laiho, M. Schiffer, and J. Unmuth-Yockey, Newtonian binding from lattice quantum gravity, *Phys. Rev. D* **103**, 114511 (2021), arXiv:2102.04492 [hep-lat].
- [40] S. Bassler, J. Laiho, M. Schiffer, and J. Unmuth-Yockey, The de Sitter Instanton from Euclidean Dynamical Triangulations, *Phys. Rev. D* **103**, 114504 (2021), arXiv:2103.06973 [hep-lat].
- [41] B. V. de Bakker and J. Smit, Curvature and scaling in 4-d dynamical triangulation, *Nucl. Phys.* **B439**, 239 (1995), arXiv:hep-lat/9407014.
- [42] J. Smit, Continuum interpretation of the dynamical-triangulation formulation of quantum Einstein gravity, *JHEP* **08**, 016, [Erratum: *JHEP* **09**, 048 (2015)], arXiv:1304.6339 [hep-lat].
- [43] J. Smit, Remarks on the quantum gravity interpretation of 4D dynamical triangulation, *Nucl. Phys. Proc. Suppl.* **53**, 786 (1997), arXiv:hep-lat/9608082.
- [44] B. V. de Bakker and J. Smit, Curvature in the crumpled phase of 4D dynamical triangulation, draft of a draft (1996).
- [45] B. V. de Bakker, Simplicial quantum gravity, (1995), arXiv:hep-lat/9508006.
- [46] A. Bonanno and F. Saueressig, Stability properties of Regular Black Holes, (2022), arXiv:2211.09192 [gr-qc].
- [47] G. Chapline, E. Hohlfeld, R. B. Laughlin, and D. I. Santiago, Quantum phase transitions and the breakdown of classical general relativity, *Int. J. Mod. Phys. A* **18**, 3587 (2003), arXiv:gr-qc/0012094.
- [48] P. O. Mazur and E. Mottola, Gravitational condensate stars: An alternative to black holes, (2001), arXiv:gr-qc/0109035.
- [49] P. O. Mazur and E. Mottola, Gravitational vacuum condensate stars, *Proc. Nat. Acad. Sci.* **101**, 9545 (2004), arXiv:gr-qc/0407075.
- [50] C. Cattoen, T. Faber, and M. Visser, Gravastars must have anisotropic pressures, *Class. Quant. Grav.* **22**, 4189 (2005), arXiv:gr-qc/0505137.
- [51] P. O. Mazur and E. Mottola, Surface tension and negative pressure interior of a non-singular ‘black hole’, *Class. Quant. Grav.* **32**, 215024 (2015), arXiv:1501.03806 [gr-qc].
- [52] A. Simpson and M. Visser, Regular black holes with asymptotically Minkowski cores, *Universe* **6**, 8 (2019), arXiv:1911.01020 [gr-qc].
- [53] B. Shoshany, OGRE: An Object-Oriented General Relativity Package for Mathematica, *J. Open Source Softw.* **6**, 3416 (2021), arXiv:2109.04193 [cs.MS].
- [54] P. Bialas, Z. Burda, and D. Johnston, Condensation in the backgammon model, *Nucl. Phys. B* **493**, 505 (1997), arXiv:cond-mat/9609264.
- [55] P. Bialas, L. Bogacz, Z. Burda, and D. Johnston, Finite size scaling of the balls in boxes model, *Nucl.Phys.* **B575**, 599 (2000), arXiv:hep-lat/9910047 [hep-lat].
- [56] S. W. Hawking and D. N. Page, Thermodynamics of Black Holes in anti-De Sitter Space, *Commun. Math. Phys.* **87**, 577 (1983).
- [57] C. W. Misner, K. S. Thorne, and J. A. Wheeler, *Gravitation* (W. H. Freeman, San Francisco, 1973).
- [58] G. W. Gibbons and S. W. Hawking, Action Integrals and Partition Functions in Quantum Gravity, *Phys. Rev. D* **15**, 2752 (1977).
- [59] S. A. Hayward, Formation and evaporation of regular black holes, *Phys. Rev. Lett.* **96**, 031103 (2006), arXiv:gr-qc/0506126.
- [60] K. Schwarzschild, On the gravitational field of a mass point according to Einstein’s theory, *Sitzungsber. Preuss. Akad. Wiss. Berlin (Math. Phys.)* **1916**, 189 (1916), arXiv:physics/9905030.
- [61] T. Rothman, Editor’s Note on J. Droste, *Gen.Rel.Grav.* **34**, 1541 (2002).

- [62] C. H. McGruder and B. W. VanDerMeer, The 1916 PhD Thesis of Johannes Droste and the Discovery of Gravitational Repulsion, (2018), arXiv:1801.07592 [physics.hist-ph].
- [63] M. D. Kruskal, Maximal extension of Schwarzschild metric, Phys. Rev. **119**, 1743 (1960).
- [64] G. Szekeres, On the singularities of a Riemannian manifold, Publ. Math. Debrecen **7**, 285 (1960).
- [65] J. Cheeger, W. Muller, and R. Schrader, On the Curvature of Piecewise Flat Spaces, Commun.Math.Phys. **92**, 405 (1984).
- [66] R. Friedberg and T. Lee, Derivation of Regge's Action From Einstein's Theory of General Relativity, Nucl.Phys. **B242**, 145 (1984).
- [67] S. Bilke, Z. Burda, A. Krzywicki, B. Petersson, K. Petrov, J. Tabaczek, and G. Thorleifsson, The Strong coupling expansion in simplicial quantum gravity, Nucl. Phys. B Proc. Suppl. **73**, 798 (1999), arXiv:hep-lat/9809088.